2022-11-01

Out of phase Quaternary uplift-rate changes reveal normal fault interaction, implied by deformed marine palaeoshorelines

Meschis, M
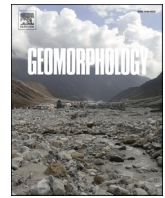
http://hdl.handle.net/10026.1/19772

Out of phase Quaternary uplift-rate changes reveal normal fault interaction, implied by deformed marine palaeoshorelines

M. Meschis [a,b,*], G.P. Roberts [a], J. Robertson [a], Z.K. Mildon [c], D. Sahy [d], R. Goswami [e],
C. Sgambato [a,f], J. Faure Walker [f], A.M. Michetti [g,h], F. Iezzi [i]

[a] Department of Earth and Planetary Sciences, Birkbeck, University of London, London, UK
[b] Istituto Nazionale di Geofisica e Vulcanologia, Sezione di Palermo, via Ugo La Malfa, 153, 90146 Palermo, Italy
[c] School of Geography, Earth and Environmental Sciences, University of Plymouth, Drake Circus, Plymouth PL4 8AA, UK
[d] British Geological Survey, Keyworth NG12 5GG, United Kingdom
[e] Royal Dutch Shell, Netherlands
[f] Institute for Risk and Disaster Reduction, University College London, Gower Street, London, WC1E 6BT, UK
[g] Università degli Studi dell'Insubria, Como, Italy
[h] INGV, Osservatorio Vesuviano, Napoli, Italy
[i] DiSTAR-Dipartimento di Scienze della Terra, dell'Ambiente e delle Risorse Università di Napoli "Federico II", Napoli, Italy

ARTICLE INFO

ABSTRACT

We have mapped and constrained the timing of tectonically deformed uplifted Late Quaternary palaeoshorelines in the Messina Strait, southern Italy, an area above a subduction zone containing active normal faults. The palaeoshorelines are preserved from up to thirteen Late Quaternary sea-level highstands, providing a record of the deformation over this timescale (~500 ka) for the Messina-Taormina Fault, the Reggio Calabria Fault and the Armo Fault. The palaeoshorelines reveal spatial patterns of uplift through time along the strike of these normal faults, and, given the across strike arrangement of the faults, also reveal how the contribution of each fault to the regional strain-rate progressed through time. The results reveal that the uplift rates mapped within the fault hangingwalls and footwalls were not constant through time, with a marked change in the location of strain accumulation at ~50 ka. The uplift rates, once converted into throw-rates, imply that the three faults comprised similar throw-rates prior to ~50 ka (in the range 0.77–0.96 mm/yr), with the Armo and Reggio Calabria faults then switching to lower rates (0.32 mm/yr and 0.33 mm/yr respectively), whilst the Messina-Taormina Fault accelerated to 2.34 mm/yr. The regional extension rate, gained by summing the implied heave rates across the three faults, was maintained through time despite this re-organisation of local strain accumulation at ~50 ka. We explain these out-of-phase fault throw-rate changes during the constant-rate regional extension conditions as due to interactions between these upper plate normal faults. We finally discuss how fault throw-rates changing through time may affect a long-term seismic hazard assessment within active normal fault systems.

1. Introduction

Knowledge of tectonic uplift rates that extend over multiple seismic cycles has been derived by investigating preserved palaeoshorelines from seismically deforming upper plates above subduction zones such as Western Burma, South America, Japan, southern Italy and Greece (e.g. González-Alfaro et al., 2018; Ott et al., 2019; Roberts et al., 2009; Roberts et al., 2013; Robertson et al., 2019; Saillard et al., 2009; Shikakura, 2014; Shyu et al., 2018). Such studies can provide continuous along-strike profiles of deformation rate of faults responsible for the

uplift over different timescales, and across multiple faults. However, such information has rarely been used to constrain how neighbouring faults share the task of accommodating the regional strain-rate over tens to hundreds of thousands of years, providing information on the dynamics of crustal deformation. For northern and central Calabria, Italy, an area located in the upper plate of the Ionian Subduction Zone, observations of knickpoints in rivers crossing faults have been used to suggest that some faults change their slip-rates over the last 300 ka (Quye-sawyer et al., 2021; Roda-Boluda and Whittaker, 2017). This information provides important new insights that hint at the larger scale

---

LEGEND

Inner edges and Age (kyr)

0	50	12	478
1	76	13	525
2	100	14	550
3a	119	15	560
3	125	16	590
4	175	17	620
5	200	18	695
6	217	19	740
7	240	20	800
8	285	21	855
9	310	22	980
10	340		
11	410		

★ 1908 Mw 7.1 earthquake (Aloisi et al., 2013)

■ Age controls by Balescu et al., 1997; Antonioli et al., 2006 and Aloisi et al., 2013

■ Coral *cladocora caespitosa* dating from this study

1 Numberd topographic profile

• Mapped inner edge

···· 125 ka palaeo-shoreline

⌐ Normal fault

Trace of topographic profiles

10 km

N

Sicily

Tyrrhenian Sea

Capo Peloro

Age control

Scilla Fault

Calabria

Messina Fault

Messina

SM 3

14
15
16
17

Coral sample 15abc, 16, 17

Reggio Calabria

Age control

Reggio Calabria Fault

Messina Strait

SM 1a

SM 1b

Nizza di Sicilia

Armo Fault

18
19
20
21
22

Age control

38°0'0"N

SM 2

38°0'0"N

SM 1c

Fig. 2

Messina-Taormina Fault

Taormina

Age control

12

13

SM 1d

15°13'31"E

Ionian Sea

Inset A

A — Tyrrhenian Sea — Sicily — Messina Strait — Calabria — B

SL

0

15 (km)

Eurasian crust — Ionian crust

(modified from Ghisetti, 1984)

Inset B

East Crati Fault

Calabria

Serre Fault

Cittanova Fault

Etna

Sicily

A

B

Ionian Subduction Zone

(caption on next page)

Fig. 1. Map of the investigated area. Sketched fault map of the Messina Strait is shown. Locations of several topographic profiles across the Messina-Taormina Fault, the Reggio Calabria Fault and the Armo Fault. Locations of age controls are shown from new $^{234}U/^{230}Th$ coral ages and from literature (Tables 1 and 2). Inner edges are shown with different coloured dots indicating refined ages (Table 3). Inset A, modified from Ghisetti (1984), shows a sketched structural scheme of the Messina Strait, accommodating ongoing crustal extension of ~3 mm/yr (Serpelloni et al., 2010). Inset B shows Quaternary active normal faults within the Calabrian Arc. Zoom in on these locations (dotted black squares) are shown in supplementary materials (Fig. SM 1, SM 2 and SM 3).

dynamic processes that occur in such extensional settings above subduction zones. However, these studies did not concentrate on whether fault slip-rate changes were associated with changes in regional extensional rates, and the timing of changes was relatively imprecise as results came from an inversion of river profile data and not absolute dating of deformed horizons. Hence, it is unclear how the slip-rate changes over the Middle to Late Pleistocene can be interpreted in terms of regional dynamics associated with the subduction processes. Such information would be useful, because elsewhere interaction between multiple across-strike active normal faults has been shown to be an important process during intraplate crustal extension located within zones of convergence between colliding tectonic plates, and other tectonic settings; the details of the interaction, revealed by data on how the faults experience changes in slip-rate through time, are essential to understand the dynamics governing the overall deformation (Anders and Schlische, 1989; Contreras et al., 2000; Cowie and Roberts, 2001; Cowie and Shipton, 1998; Gupta et al., 1998; Mcleod et al., 2000; Nicol et al., 2006; Roberts et al., 2002). The Messina Strait is located on the extending upper plate of the Ionian Subduction Zone (ISZ; southern Italy) (Malinverno and Ryan, 1986), within an area of active convergence between the African and Eurasian plates, and is considered one of the most tectonically-active regions of the entire Mediterranean (Monaco and Tortorici, 2000; Serpelloni et al., 2010) (Fig. 1). The geodetically constrained crustal extension rate of ~3 mm/yr is accommodated within the Messina Strait by synthetic and antithetic normal faults (Doglioni et al., 2012; Monaco and Tortorici, 2000; Serpelloni et al., 2010) (Fig. 1), which hosted the most powerful recorded earthquakes during the 20th and the 21st centuries in Europe to date (1908 Messina Earthquake – M 7.1; e.g. Aloisi et al., 2013; Meschis et al., 2019; Valensise and Pantosti, 1992). However, Late Quaternary crustal deformation rates associated with these seismically active normal faults are poorly constrained and so the processes that control the dynamics of the deformation are poorly understood. Uplifted Late Quaternary palaeoshorelines suggest Middle to Late Pleistocene deformation (Catalano and De Guidi, 2003; Stewart et al., 1997; Valensise and Pantosti, 1992), but rates of activity through time, and the likely effects of interaction on the closely-spaced normal faults are still unclear. Indeed, some have even questioned if these faults are still active (Argnani et al., 2009). Previous studies have shown deformed uplifted Late Quaternary palaeoshorelines mapped along the strike of the offshore Messina-Taormina Fault on its onshore footwall, between Messina town and Taormina town (Catalano and De Guidi, 2003; Pavano et al., 2016; Stewart et al., 1997). Likewise, major capable onshore normal faults, such as the Reggio Calabria Fault and the Armo Fault, and their influence on the "regional" uplift throughout the Quaternary on the Calabrian side, have been previously investigated by studying sequences of uplifted Late Quaternary palaeoshorelines both on their footwalls and hangingwalls (Catalano et al., 2003; Miyauchi et al., 1994; Monaco and Tortorici, 2000; Valensise and Pantosti, 1992). Yet, for one of the most seismically active regions in the Mediterranean realm like the fault-bounded Messina Strait, uncertainties remain on (i) how slip-rates on these crustal-scale faults compare between neighbouring structures, (ii) whether the faults interact and hence (iii) what controls the changes in the deformation through time in response to the tectonic forcing.

In this paper we use flights of marine terraces to reconstruct the recent tectonic and geomorphological evolution of southernmost Calabria and northern Sicily. Uplift rates of the footwall and hanging wall blocks of normal faults, several tens of kilometres in length, in the two sides of the Messina Strait (Fig. 1), and the fault throw rates are refined

using (i) a synchronous correlation approach driven by age controls from the literature and (ii) new absolute dated age controls. From the modelling, an uplift rate change at 50 ka is identified and we demonstrate synchronous, out-of-phase changes in uplift rate, showing how these relate to slip-rate changes and regional extension rate and hence the regional processes of the subduction system. We finally discuss implications for seismic hazard.

2. The geological background of the Messina Strait region

The investigated area lies within the uplifting and seismically extending Calabrian-Peloritani forearc, where the origin of the "regional" signal of uplift, associated with either with the Ionian subduction process (Malinverno and Ryan, 1986) or with mantle upwelling (Gvirtzman and Nur, 1999a, 1999b), is still debated, In particular, the Messina Strait, separating Calabria from Sicily, southern Italy, is a down-faulted graben between inward-dipping Quaternary normal faults, deforming a pre-existing fold and thrust belt made of Palaeozoic, Mesozoic and Cenozoic rock formations interposed during Alpine thrusting (Ghisetti, 1984; Malinverno and Ryan, 1986; Fig. 1). This strait is bounded by active normal faults onshore (Catalano et al., 2003; Monaco and Tortorici, 2000; Stewart et al., 1997) and offshore (De Guidi et al., 2003; Doglioni et al., 2012; Meschis et al., 2019). In particular, the offshore and E-dipping Messina-Taormina Fault offsets pre-Quaternary basement and has propagated upwards to produce a fault-related anticline on its footwall, from Messina town to Taormina town (Catalano et al., 2003; Meschis et al., 2019; Pavano et al., 2016; Stewart et al., 1997; Fig. 1). This fault has deformed the Late Quaternary-Holocene palaeoshorelines outcropping onshore on the Sicilian side of the Messina Strait (Catalano et al., 2003; De Guidi et al., 2003; Pavano et al., 2016; Stewart et al., 1997). Likewise, W-dipping antithetic normal faults, such as the Armo Fault and the Reggio Calabria Fault, control the coastline topography on the Calabrian side of the Messina Strait, deforming the Palaeozoic crystalline thrust sheets and its clastic Cenozoic cover, with the Middle-Late Pleistocene shallow marine deposits, progressively onlapping on fault planes and suggesting persistent faulting (Ghisetti, 1984; Monaco and Tortorici, 2000).

Existing ages of marine terraces mapped in the Messina Strait are briefly summarized here and in Table 1. In particular, along the mapped palaeoshorelines on the footwall of the Messina-Taormina Fault, shallow marine shells have been dated close to Taormina town, identifying the 125 ka (MIS 5e) palaeoshoreline (Antonioli et al., 2006b). By using the Electron Spin Resonance technique on marine mollusc shells such as *Patella* and *Venerupid,* shallow marine deposits have been dated (Table 1). Moreover, eolian non-fossiliferous sediments have been dated north of Reggio Calabria (Fig. 1) by applying a thermoluminescence dating technique, identifying the 50 ka palaeoshoreline (Balescu et al., 1997). Thermoluminescence has also been used to date shallow marine deposits from marine terraces, south of Reggio Calabria, identifying the 125 ka (MIS 5e) marine terrace (Balescu et al., 1997). South of Reggio Calabria and within the hangingwall of the Armo Fault, *Persististrombus latus* a fossil that is commonly used to date marine oxygen isotope stage 5 deposits in the coasts of Italy, have been collected in situ from within shallow sea deposits and used to identify the 125 ka palaeoshoreline (Aloisi et al., 2013; Antonioli et al., 2006a; Antonioli et al., 2006b; Dumas et al., 2005; Ferranti et al., 2006; Miyauchi et al., 1994).

Table 1

Age controls from literature used to drive our synchronous correlation approach for each investigated fault. Note that elevations palaeoshorelines from this study and previous ones used as age controls may differ because samples may have been collected in a different part of the same terrace (Profiles 12 and 14).

Reference	Dating method	Dated sample description	Profile number	Reported age (kyrs)	Assigned highstand (ka)	Palaeoshoreline elevations (m a.s.l)
Antonioli et al., 2006b	Electron Spin Resonance technique	*"Based on ESR methodology applied to a Patella and venerupid shells (sample nos. K-4343 and K-4244, University of Koln) collected at + 105 m, we obtained ages of 76.47̠7.2 and 103.37̠12.5 ka. If the age is calculated using a constant Uranium-uptake model, the value is 124.57̠15.0 ka. We attribute these terraces to MIS 5, probably MIS 5.5 (Figs. 3C, D and 6)."* 33 S 555865 E – 4189073 N	12	100–125	125	130
Balescu et al., 1997	Thermo-luminescence dating	*"Non-fossiliferous eolian sand from a dune associated with a post-last interglacial paleoshoreline culminating at an altitude of 43 m a.s.l.(see sample AC 21)."* 33 S 556099 E – 4229321 N	14	59 ± 7	50	34
Balescu et al., 1997	Thermo-luminescence dating	*"The two fossiliferous reference samples (RA21 and BO21) from the 129 m Tyrrhenian terrace at Ravagnese and Bovetto yield corrected TL ages of 116̠ + 13 ka and 116̠ + 12 ka, respectively. These are in better agreement with the expected substage 5e age."* 33 S 558794 E – 4215520 N 33 S 559457 E – 4212227 N	18–19	125	125	125–132
Aloisi et al., 2013	Geomorphological correlation	*"In southernmost Calabria, the terrace attributed to the Marine Isotopic Stage (MIS) 5.5, which is dated at 125 ka BP and can be fairly well recognized due to its palaeontological content (Ferranti et al., 2006), has its inner margin, a close proxy for the palaeo-sea level, lying at elevations between ~130 and ~180 m (Dumas and Raffy 2004)"* 33 S 557433 E – 4206708 N	22	125	125	175

3. Methods

In this section, we present approaches and methodologies used in this work to refine fault-related deformation rates within the crustal extending Messina Strait.

3.1. Topographic analysis: DEMs and fieldwork to map palaeoshorelines

Detailed topographic and geomorphological analysis has been carried out using 10 m high resolution DEMs (Tarquini et al., 2012) to create serial topographic profiles along the strikes of the Messina-Taormina Fault, the Armo Fault and the Reggio Calabria Fault (Fig. 1 and Supplmementary Materials (SM) Figs. SM 1–3). These topographic profiles were chosen where the geomorphology of palaeoshorelines is appropriate due to their preservation from erosion (e.g. Fig. 2) as well as being close to previously mapped locations, that have been used as a guide (Aloisi et al., 2013; Antonioli et al., 2006a; Antonioli et al., 2006b; Balescu et al., 1997; Catalano et al., 2003; Catalano and De Guidi, 2003; De Guidi et al., 2003). It is important to note that in this study palaeoshorelines are identified as the inner edge of a marine terrace where palaeo mean sea level would stand during a sea level highstand, ruling out distal deposits which may be formed at tens meters of water depth from the inner edge. The topographic profiles cover the lengths of the faults, from their centres towards their lateral tips, but complete coverage along strike has not been achieved as the Reggio-Calabria Fault goes offshore in the SW and palaeoshorelines are unclear and poorly preserved due to erosion in the high topography at the NE-end of the Armo Fault. For the Messina-Taormina Fault along strike coverage has been achieved, and palaeoshoreline elevations have been measured along the entire fault length (Fig. 1). In particular, we have been identifying both erosional and depositional marine terraces and erosional coastal landforms such as truncation surfaces, beach pebbles/cobbles, marine conglomerates, flat-surfaces cut into bedrock by erosion of wave action with evidence of lithophagid borings and millholes (or marine erosion pan) that suggest deposition and re-working in a shoreface environment (Armijo et al., 1996; Ferranti et al., 2006; Miller and Mason, 1994; Robertson et al., 2019; Robertson et al., 2020). They are unconformably overlying the Palaeozoic crystalline thrust sheets and/or Mesozoic/Neogene limestones (Figs. 2 and 3). It is important to highlight that all these features form within the subtidal/intertidal zone a few decimetres to some metres down-dip of the inner edge of the marine terrace. Indeed, gently-sloping surfaces have been interpreted as palaeoshoreface surfaces cut by wave-action and bounded up-dip by fault scarp-like resembling palaeo-sea-cliffs, following previous marine terrace investigations (Armijo et al., 1996; Roberts et al., 2009; Roberts et al., 2013; Robertson et al., 2019, 2020).

Once palaeoshorelines and their associated palaeoshoreface deposits and wave-cut platforms were identified in the field (Fig. 2), their UTM coordinates and elevation were recorded using a hand-held GPS with barometric altimeters with a precision of ±3 m), with the barometer calibrated to sea-level every few hours. Field-based palaeoshoreline elevations were georeferenced onto DEMs to confirm their reliability, following approaches from recent studies (Meschis et al., 2018; Meschis et al., 2020; Roberts et al., 2013; Robertson et al., 2019).

3.2. $^{234}U/^{230}Th$ coral dating

New age controls have been obtained through dating of corals with the $^{234}U/^{230}Th$ dating technique. In particular, dated corals allow us to place some constraints on the age for a prominent marine terrace on the footwall of the Reggio Calabria Fault (Table 2). The corals we collected were from a calcarenite boulder within shallow marine deposits, from a footwall terrace yet mapped in this paper along our Profile 16 and by other authors along the hangingwall cut-off of the Reggio Calabria Fault (Catalano et al., 2003) (Fig. 1). We then carried out $^{234}U/^{230}Th$ dating at the Geochronology and Tracers Facility of the British Geological Survey, Keyworth, UK. Here, we use total dissolution methods as outlined by Crémière et al. (2016), with ratios of the isotopes measured on a Neptune Plus MC-ICP-MS (Multi-Collector Inductively Coupled Plasma Mass Spectrometer). We undertook coral preparation and cleaning, a critical phase before $^{234}U/^{230}Th$ analysis, at Birkbeck College. In particular, we isolated millimetre-scale fragments of pure aragonitic corallite, carefully selected and systematically cleaned. We removed as much as possible of any material showing evidence of alteration and/or detrital matrix on the outside of the corallite wall. We did this, following approaches from previous studies (e.g. Meschis et al., 2020; Roberts
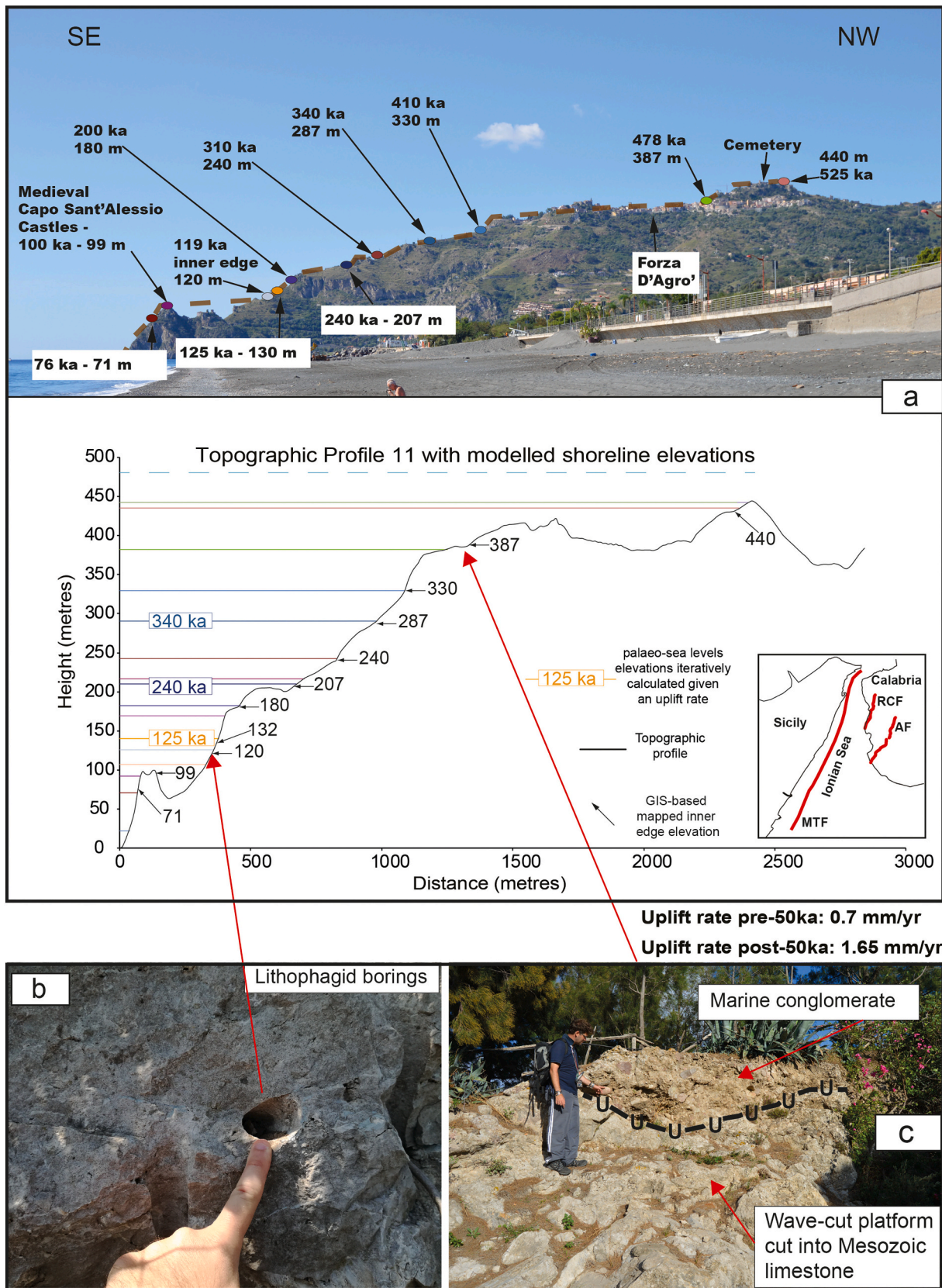
Fig. 2. (a) A sequence of uplifted marine terraces is shown on the Sicilian coast, in particular on the footwall of the offshore Messina-Taormina Fault. Inner edges of marine terraces have been mapped in the field (coloured dots) and on DEMs (see topographic profile), and refined ages are assigned using a synchronous correlation approach. Field evidence of palaeoshorelines such as lithophagid borings (b) and a Mesozoic limestone-made wave-cut platform overlies by shallow marine conglomerate identifying an unconformity (c) are shown. Location of this profile is also shown in Fig. 1.
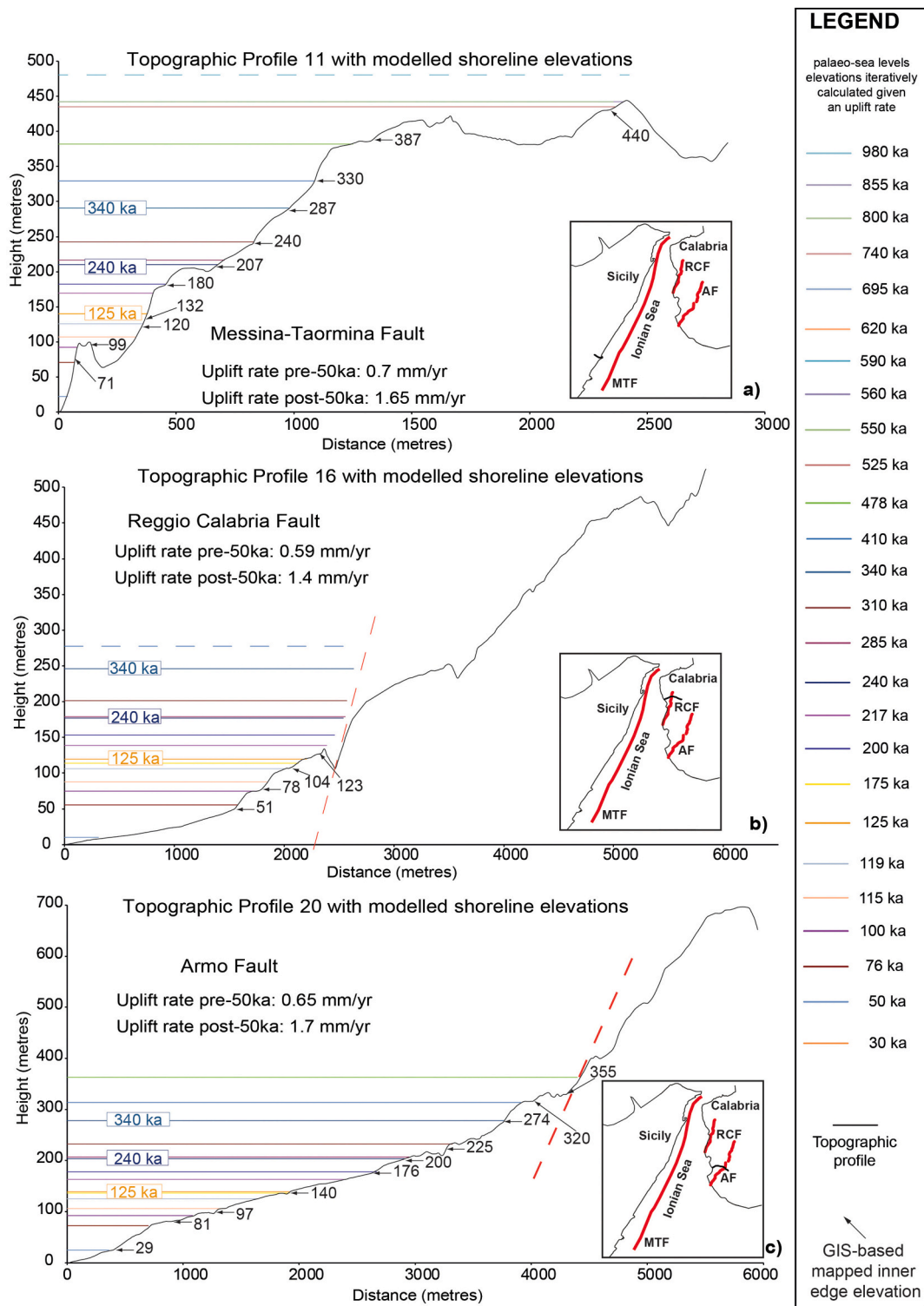
Fig. 3. Topographic profiles for each investigated active fault derived by using 10-m high resolution DEMs (Tarquini et al., 2012), showing modelled palaeoshoreline elevations. Sea-level highstands, identifying predicting palaeoshoreline elevations, are represented by coloured lines that are calculated by iterating values of uplift rate to find the best match with the mapped (numbered arrows) palaeoshorelines. All topographic profiles (13 profiles for the Messina-Taormina Fault, 4 profiles for the Reggio Calabria Fault and 5 profiles for the Armo Fault) are shown on Figs. SM 4–10). Inner edge elevations with refined ages are also shown in Table 3.

et al., 2009; Robertson et al., 2020), mechanically using a scalpel under a microscope and/or chemically by washing the wall with HCl (10 %) for 5–10 s, followed by thorough rinsing with ultrapure water. Moreover, we separated and removed coral septa from the corallite wall because they are thinner and more prone to diagenetic alteration (Roberts et al., 2009; Robertson et al., 2020). Following other studies (e.g. Meschis

et al., 2020), we also examined both bulk corallite wall fragments (2–10 mg) and powdered subsamples obtained using a computer-controlled drill equipped with a 200 μm drill bit in order to avoid any portion of the coral that showed discolouration or other evidence of alteration. Note that samples 1–14 have shown evidence of open system and then discarded from this study yet samples 15–17 allow us to obtain a relative

Table 2

Measurements of ^{234}U/^{230}Th Isotope ratios of coral samples collected on the footwall of the Reggio Calabria Fault (see Fig. 1 for location). Note that samples 1–14 have shown evidence of open system and the discarded from this study.

Sample	Weight (mg)	U (ppm)	Th (ppm)	(^{230}Th/^{232}Th)	(^{232}Th/^{238}U)	±2 s (%)	(^{230}Th/^{238}U)	±2 s (%)	(^{234}U/^{238}U)	±2 s (%)	Age (ky) ± 2 s (abs) (ky)	δ^{234}U$_i$
1	14.02	3.72	0.030	472.6	0.0026074	0.05	1.23218	0.22	1.1095	0.12	–	–
2	9.21	3.30	0.019	625.7	0.0019222	0.06	1.20263	0.23	1.0899	0.14	–	–
3	2.97	3.74	0.013	1162.9	0.0011266	0.07	1.31008	0.25	1.1206	0.19	–	–
4	3.63	3.21	0.014	949.8	0.0013820	0.07	1.31259	0.25	1.1225	0.17	–	–
5	8.83	3.79	0.002	8338.5	0.0001454	0.08	1.21234	0.23	1.1020	0.13	–	–
6	11.23	3.99	0.002	6782.8	0.0001758	0.11	1.19235	0.23	1.0965	0.12	–	–
7	7.00	3.29	0.011	1444.5	0.0011158	0.06	1.61180	0.23	1.2496	0.14	–	–
8	10.83	3.49	0.001	10,757.9	0.0001114	0.10	1.19885	0.22	1.0966	0.14	–	–
9	4.05	4.63	0.014	1954.2	0.0009629	0.06	1.88163	0.23	1.3990	0.14	–	–
10	15.18	4.79	0.014	1514.0	0.0009349	0.05	1.41548	0.22	1.2486	0.11	–	–
11	11.80	4.87	0.004	5407.0	0.0002680	0.07	1.44911	0.22	1.2987	0.11	–	–
12	6.84	4.89	0.042	525.7	0.0028140	0.07	1.47943	0.23	1.1141	0.13	–	–
13	5.18	4.36	0.045	442.7	0.0033686	0.07	1.49121	0.23	1.1190	0.13	–	–
14	7.72	6.13	0.071	380.9	0.0037952	0.07	1.44556	0.23	1.1240	0.13	–	–
15a	22.85	3.47	0.002	4424.9	0.0002269	0.07	1.00418	0.22	1.0150	0.12	449 ± 17	53.20
15b	11.67	3.68	0.003	3891.0	0.0002585	0.05	1.00568	0.27	1.0175	0.19	438 ± 21	60.04
15c	15.70	3.53	0.002	6543.8	0.0001533	0.05	1.00325	0.27	1.0152	0.16	441 ± 20	52.83
16	5.32	2.82	0.003	2912.9	0.0003436	0.09	1.00073	0.26	1.0229	0.16	384 ± 11	67.74
17	8.31	3.84	0.009	1308.9	0.0007713	0.07	1.00952	0.23	1.0158	0.13	480 ± 25	61.15

age control used to refine rates of crustal deformation. Finally, we highlight that our terrace modelling by applying a synchronous correlation approach (described in the next section) is driven by age controls from literature as shown in Table 1.

3.3. Synchronous correlation approach for multiple palaeoshorelines and multiple sea-level highstands modelling

This technique has been used within the Mediterranean realm and elsewhere (Meschis et al., 2018; Meschis et al., 2020; Pedoja et al., 2018; Roberts et al., 2009; Roberts et al., 2013; Robertson et al., 2019; De Santis et al., 2021). This technique is built on the concept that sea-level highstands, which are thought to produce palaeoshorelines (Lajoie, 1986), are unequally-spaced in time, implying that for a constant uplift rate through time, palaeoshorelines will be unequally-spaced in elevation (Houghton et al., 2003; Roberts et al., 2009). To use this approach, it is important to obtain at least one age for a palaeoshoreline across the investigated area. The age control drives the iteration of uplift rate to replicate the elevation of the dated palaeoshoreline, but also predicts the elevations of palaeoshorelines from other Quaternary sea-level highstands, for comparison with the elevations of mapped yet un-dated palaeoshorelines. The modelling can involve either a single constant uplift rate or can include multiple changes in uplift rate at times that can be specified by the user. For example, Roberts et al. (2009), studying central Greece, found that a single change in uplift rate through time was necessary to replicate measured palaeoshoreline elevations, whereas Roberts et al. (2013), studying central Calabria (southern Italy), found that no change in uplift rate was needed and a constant uplift rate throughout the Late Quaternary could explain the measured palaeoshorelines. In summary, this approach tests if un-dated palaeoshorelines can be modelled by iterated uplift rates implied by the dated palaeoshorelines. This iteration is enabled by a "Terrace Calculator" built in Excel, available in the literature where data from sea-level highstands are input (Roberts et al., 2013). The "Terrace Calculator" uses an input uplift rate (UR), which is iterated to calculate the predicted elevations (PE) of all sea-level highstands using the age of the highstands (T) and the sea level elevations of each highstand (SLE) using this formula: $PE = (UR \times T) + SLE$ (e.g. Meschis et al., 2020). More particularly, the uplift for the whole profile is iterated based on the palaeoshoreline with the age control such that the measured elevation matches that predicted by the "Terrace Calculator". Then the measured elevations are matched to the predicted elevations (within a range $+/- 10$ m) which allows undated palaeoshorelines to be allocated to sea-level highstands.

Note that iterations of uplift rates are driven by reliable and robust age controls from literature shown in Table 1. This approach forces the user to maximise the coefficient of determination (R^2 value) for linear regression analysis through data including the "measured" (or mapped) elevations of all palaeoshoreline elevations on a topographic profile (GIS analysis and field) and the "predicted" (or expected) elevations which identify sea-level highstand elevations implied by iterating uplift rate values driven by age constrains and by means of available sea-level curves for the last ~0.9–1 My (Table SM 1) (Rohling et al., 2014; Siddall et al., 2003).

We discuss how uplift-rates can be used to constrain slip-rates on the faults in the discussion section. However, note that the topographic profiles we study exist in the footwall of the Messina-Taormina Fault and the hangingwalls of the Reggio Calabria and Armo faults; this must be factored into interpretations of the throw-rates and (and slip-rates if the fault dip is known) because an increase in footwall uplift rate implies an increase in slip-rate whereas an increase in hangingwall uplift rate may imply a decrease in slip-rate given a constant background regional uplift rate.

4. Results

Table 3 shows all mapped palaeoshoreline elevations defined in this study with ages constrained by the synchronous correlation carried out in this paper; data cover the regions associated with all 3 faults we have studied across. These elevation data support the plots in Fig. 3, which are shown as examples (and Figs. SM 4–10 for our synchronous correlations applied to all topographic profiles across the 3 investigated faults), with detailed analysis of topographic profiles across the footwall of the Messina-Taormina Fault and the hangingwalls of the Armo and Reggio Calabria faults. The following sections describe the procedures we performed to gather the data in Table 3 and justify their robustness.

4.1. Check of the reproducibility of topographic measurements of palaeoshoreline elevations

We conducted a check of the consistency between the two datasets from this work of elevations of palaeoshorelines using (i) a handheld GPS with barometric altimeter in the field (Fig. 2) and (ii) digital mapping from the DEM (Fig. 3). In particular, elevation data from our DEM-based analysis were compared with elevations from our field-based palaeoshoreline mapping, also revisiting palaeoshoreline locations from the literature using them as a guide for our fieldwork.

Table 3

Mapped inner edge elevations of marine terraces from fieldwork and DEM analysis with refined ages assigned using a synchronous correlation approach are shown. Note that all UTM coordinate are projected in WG84 33°S grid zone. Note that age controls from literature used for our synchronous correlation modelling are stated by an asterisk (*) and bold-highlighted.

Profile number (sea level highstand referred to Fig. 1, SM1, SM2 and SM3)	UTM coordinate (easting)	UTM coordinate (northing)	Barometric altimeter palaeoshoreline elevations (this study) (m)	DEMs elevations (m)	Predicted elevations (m)	Our proposed age (ka)
			Messina-Taormina fault			
1 (1)	548109	4226786	–	49	43	76
1 (3)	547784	4226847	–	106	103	125
1 (7)	546450	4227164	–	140	150	240
1 (11)	546234	4227257	–	230	235	410
1 (19)	545033	4227549	–	408	410	740
1 (20)	543821	4228040	–	458	455	800
1 (21)	543645	4228146	–	487	487	855
2 (2)	546538	4223495	–	65	60	100
2 (3)	546212	4223662	107	103	103	125
2 (5)	546020	4223740	–	135	130	200
2 (7)	545475	4224092	145	144	150	240
2 (10)	545066	4224403	190	203	210	340
2 (11)	544964	4224469	245	245	235	410
2 (20)	543709	4224854	–	451	455	800
2 (22)	543263	4225009	–	531	550	980
3 (1)	544636	4219045	–	55	51	76
3 (2)	544558	4219045	80	71	69	100
3 (3)	544424	4219106	120	114	113	125
3 (7)	544151	4219170	–	155	165	240
3 (10)	543477	4219168	–	220	229	340
3 (11)	542755	4219538	–	255	256	410
3 (13)	542755	4219538	–	335	344	525
3 (21)	541347	4219715	–	518	522	855
4 (1)	543853	4216396	–	55	55	76
4 (2)	543657	4216361	–	81	73	100
4 (3)	543215	4216202	–	119	116	125
4 (10)	542883	4216095	–	235	235	340
4 (11)	542527	4216106	–	261	263	410
4 (12)	542413	4216117	–	300	305	478
5 (1)	542390	4213537	–	52	57	76
5 (3)	542162	4213570	–	114	120	125
5 (7)	541973	4213662	170	170	176	240
5 (9)	541819	4213735	210	205	199	310
5 (10)	541697	4213807	–	245	243	340
5 (11)	541555	4213895	280	280	274	410
5 (12)	540944	4214296	320	315	318	478
5 (15)	540827	4214396	–	379	368	550
5 (16)	540700	4214634	–	400	402	590
6 (1)	541118	4211552	70	70	67	76
6 (2)	541571	4212081	85	88	87	100
6 (3a)	541403	4212174	110	110	120	119
6 (3)	541325	4212245	130	125	135	125
6 (5)	541075	4212412	180	180	176	200
6 (7)	540951	4212465	–	203	203	240
6 (10)	540849	4212508	–	273	281	340
6 (11)	540702	4212602	–	335	318	410
6 (12)	540550	4212712	–	380	370	478
6 (16)	540343	4212898	–	450	466	590
7 (1)	540829	4211262	–	60	71	76
7 (3a)	540767	4211332	–	132	126	119
7 (3)	540629	4211433	138	146	141	125
7 (5)	540354	4211570	–	195	184	200
7 (7)	540271	4211615	200	203	212	240
7 (10)	540113	4211731	–	293	286	340
7 (12)	539901	4211824	375	376	386	478
7 (13)	539670	4211819	–	441	440	525
7 (17)	539365	4211905	–	517	507	620
7 (19)	539176	4212247	–	585	577	740
7 (20)	538895	4212998	–	647	635	800
8 (1)	538404	4207920	90	91	86	76
8 (3a)	538186	4208020	–	138	145	119
8 (3)	538101	4208095	–	160	160	125
8 (7)	537794	4208392	–	238	242	240
8 (10)	537526	4208634	–	328	332	340
8 (12)	537243	4208906	–	450	437	478
8 (13)	537133	4208989	–	483	495	525
8 (17)	537042	4209164	–	565	571	620
8 (18)	536946	4209421	–	605	621	695
9 (1)	534134	4203177	–	77	86	76

Table 3 (*continued*)

Profile number (sea level highstand referred to Fig. 1, SM1, SM2 and SM3)	UTM coordinate (easting)	UTM coordinate (northing)	Barometric altimeter palaeoshoreline elevations (this study) (m)	DEMs elevations (m)	Predicted elevations (m)	Our proposed age (ka)
9 (2)	533969	4203270	–	101	110	100
9 (3a)	533784	4203368	–	150	145	119
9 (3)	533598	4203466	180	173	160	125
9 (5)	533517	4203530	–	204	210	200
9 (7)	533304	4203610	–	239	242	240
9 (10)	532554	4204160	–	336	332	340
9 (11)	532245	4204392	–	385	378	410
9 (12)	532005	4204553	–	438	437	478
9 (15)	531248	4205315	–	513	506	560
9 (17)	530678	4205893	–	570	571	620
10 (1)	532055	4200306	75	75	73	76
10 (3a)	531816	4200409	–	132	129	119
10 (3)	531687	4200497	–	147	143	125
10 (7)	531388	4200659	–	212	217	240
10 (10)	530915	4200935	–	292	299	340
10 (11)	530672	4201093	320	330	340	410
10 (17)	528707	4201593	–	526	517	620
10 (18)	528425	4201643	–	564	562	695
10 (19)	528276	4201668	–	600	589	740
10 (22)	527522	4201891	–	790	783	980
11 (1)	530561	4196241	–	71	71	76
11 (2)	530542	4196245	–	99	93	100
11 (3a)	530297	4196212	115	120	126	119
11 (3)	530298	4196229	130	132	140	125
11 (5)	530189	4196208	165	180	183	200
11 (7)	530094	4196212	220	207	211	240
11 (9)	530094	4196230	–	240	243	310
11 (10)	529688	4196254	290	287	291	340
11 (11)	529598	4196352	330	330	330	410
11 (12)	529388	4196416	375	387	382	478
11 (13)	528566	4197040	445	440	435	525
12 (1)	526025	4188873	53	48	53	76
12 (3)*	**525844**	**4189113**	**–**	**122**	**118**	**125**
12 (7)	525726	4189254	177	173	177	240
12 (10)	525242	4189615	245	255	247	340
12 (13)	524521	4190029	–	375	373	525
12 (16)	523551	4190611	–	405	412	590
13 (2)	519946	4185828	–	58	59	100
13 (3)	519653	4185868	–	102	101	125
13 (9)	519358	4186056	–	158	162	310
13 (10)	518890	4186329	–	201	204	340
13 (17)	518174	4186534	–	349	353	620
13 (19)	517893	4186605	–	393	396	740
			Reggio Calabria fault			
14 (0)*	**556796**	**4226515**	**30**	**34**	**40**	**50**
14 (1)	557360	4226749	–	97	94	76
14 (2)	557599	4226872	112	115	120	100
14 (3a)	558440	4227121	150	150	157	119
14 (3)	558999	4227289	174	173	174	125
14 (7)	560866	4227076	–	270	266	240
14 (9)	561574	4227195	–	312	312	310
14 (10)	561738	4227283	–	362	366	340
14 (11)	562119	4227661	–	420	419	410
15 (0)	556979	4225258	–	25	23	50
15 (1)	558322	4225768	–	71	70	76
15 (2)	558985	4226063	–	99	91	100
15 (3)	559098	4226092	–	135	138	125
16 (1)	558085	4224704	–	51	56	76
16 (2)	558289	4224793	–	78	75	100
16 (3a)	558522	4224917	110	104	106	119
16 (3)	558807	4224969	123	123	119	125
17 (1)	558189	4222423	–	57	51	76
17 (2)	558376	4222319	–	72	69	100
17 (3)	558465	4222285	–	113	113	125
			Armo fault			
18 (1)	558088	4214726	–	54	57	76
18 (2)	558514	4215190	–	81	76	100
18 (3a)	558611	4215468	–	107	106	119
18 (3)*	**558794**	**4215520**	**126**	**125**	**120**	**125**
18 (7)	559028	4215626	168	165	174	240
18 (10)	559867	4215297	250	245	240	340
18 (11)	560304	4215184	–	272	269	410
18 (12)	561116	4215169	320	306	312	478
19 (1)	558388	4212677	–	61	65	76

Table 3 (*continued*)

Profile number (sea level highstand referred to Fig. 1, SM1, SM2 and SM3)	UTM coordinate (easting)	UTM coordinate (northing)	Barometric altimeter palaeoshoreline elevations (this study) (m)	DEMs elevations (m)	Predicted elevations (m)	Our proposed age (ka)
19 (2)	558788	4212503	–	89	84	100
19 (3)*	**559457**	**4212227**	**135**	**132**	**129**	**125**
19 (5)	559740	4212193	156	156	164	200
19 (7)	559960	4212168	180	172	188	240
19 (10)	560536	4212257	259	255	258	340
19 (11)	560981	4212355	290	284	290	410
19 (12)	561742	4212200	–	345	336	478
20 (0)	557767	4211086	–	29	25	50
20 (1)	558360	4211362	–	81	72	76
20 (2)	558550	4211458	–	97	93	100
20 (3)	559175	4211417	–	140	139	125
20 (5)	559873	4211187	–	176	178	200
20 (7)	560244	4211110	205	200	204	240
20 (9)	560512	4211073	230	225	232	310
20 (10)	560926	4210934	270	274	279	340
20 (11)	561086	4210765	–	320	314	410
20 (12)	561431	4210585	355	355	363	478
21 (0)	557753	4208702	–	28	35	50
21 (1)	557920	4208377	–	78	85	76
21 (2)	558053	4208283	–	110	108	100
21 (3)	558202	4208194	–	158	156	125
22 (0)	556638	4207631	50	54	50	50
22 (1)	556962	4207191	–	100	103	76
22 (3a)	557383	4206748	157	163	164	119
22 (3)*	**557433**	**4206708**	**175**	**180**	**179**	**125**

Comparison of the elevations shows a robust correlation with R^2 values >0.99 (Fig. 4). This suggests that: (i) elevations measured elsewhere in DEMs are likely to be reliable and (ii) that our mapping is consistent with mapping data published by other authors in terms of locations and elevations of palaeoshorelines (Antonioli et al., 2006b; Catalano et al., 2003; Catalano and De Guidi, 2003; De Guidi et al., 2003; Miyauchi et al., 1994), but ages of un-dated marine terraces may need to be reviewed.

4.2. Comparison of the elevations of measured palaeoshorelines and the elevations of palaeoshorelines predicted by iterated uplift rate scenarios

We use age controls (Tables 1 and 2) combined with the Terrace Calculator to iterate uplift rates to obtain a correlation between mapped palaeoshoreline elevations and predicted sea level highstand elevations for undated yet mapped palaeoshorelines. This allows us to investigate palaeoshoreline elevations and uplift rates along the strike of the 3 investigated faults. In particular, uplift rates were iterated (see Figs. SM 4–10) and linear regression was used to assess the robustness of correlations between the predicted elevations iteratively calculated given (i) an uplift rate value driven by either new age controls from this study and from literature (Aloisi et al., 2013; Antonioli et al., 2006b; Balescu et al., 1997; Tables 1 and 2) and (ii) fixed values for sea level relative to present-day sea-level for several well-known highstands (Table SM 1; Rohling et al., 2014; Siddall et al., 2003) and those mapped in DEMs (Figs. 3 and Figs. SM 4–10). Note that uncertainty associated with sea level curves through the Late Quaternary differ depending on the sea level curve used. For those used in this work the stated uncertainties are 12 m and 6 m (Rohling et al., 2014; Siddall et al., 2003). These values are nearly in the same order of the 10-m DEM resolution and does not affect significantly our refined chronology of marine terraces. Moreover, in a previous study (Robertson et al., 2019) where similarly a synchronous correlation is applied to study a sequence of uplifted marine terraces deformed by normal faulting activity (with very similar uplift rate values), different sea level curves were tested for sensitivity test to show if differences on final results on derived uplift rates were found. In particular, it is shown that regardless of the sea level curves used (e.g. Siddall et al., 2003; Waelbroeck et al., 2002), very similar results for uplift rates and then tectonic implications were obtained. It is also

important to highlight that Siddall et al. (2003) better describes sea-level changes through the Middle Pleistocene to the present for the Mediterranean Sea.

Fig. 5 shows correlations between measured and predicted palaeoshorelines elevations using both constant (Fig. 5a, b, c and Figs. SM 11–18) and fluctuating uplift rates through time (Fig. 5d, e, f and Figs. SM 11–18). Initially, we assumed constant uplift rates through time. Correlations between measured and predicted palaeoshoreline elevations produced reasonably good correlations (R^2 values in the range of 0.9677–0.9954; $y = 0.9665\times$ to $y = 0.903\times$; Fig. 5a, b and c). However, after a number of iterations, we found that correlations improved if we included changing uplift-rates through time, specifically a change in uplift-rate on all 3 faults at 50 ka (R^2 values >0.9985; $y = 0.9697\times$ to $y = 1.0167\times$ – Fig. 5d, e and f), with a very robust correlation for all topographic profiles ($R^2 > 0.99$ - Fig. 5g, h and i). Coefficient of determination, R^2, for each topographic profile (1−22) for the fluctuating uplift rate scenario is higher compared to the constant uplift rate scenario (Figs. SM 11–18). We did not enforce this value of 50 ka into the calculations. Instead, this value arose as it produced the best fit for each of the 3 faults. The fact that the 50 ka value produces the best fits on 3 separate faults in 3 separate calculations suggests that it may well signify a major re-organisation of strain distribution in the rift. The result of our analyses tested this hypothesis by exploring the implications of this possibility. The results of assuming changing rates at 50 ka are detailed in Figs. 5 and 6.

Fig. 6a, b and c show spatial variations of uplift along the strikes of the investigated normal faults recorded by the geometry of the palaeoshorelines. The fact that the palaeoshorelines are tilted and/or folded along strike suggests faulting activity spanning the Middle-Late Pleistocene. Furthermore, Fig. 6d, e and f imply that uplift rates vary along the strike of the faults and through time. Note that our interpretation of the uplift rates for the footwall of the Messina-Taormina Fault differs from that of Pavano et al. (2016) who utilise elevation data and uplift rates from Catalano et al. (2003), Catalano et al. (2003) and De Guidi et al. (2002). Similar to our interpretation, Pavano et al. (2016) show uplift changing along the coast with minima in the NE and SW near Capo Peloro and Taormina respectively, and a maximum near to Nizza di Sicilia (located in Fig. 1), however they suggest the MIS 5e terrace
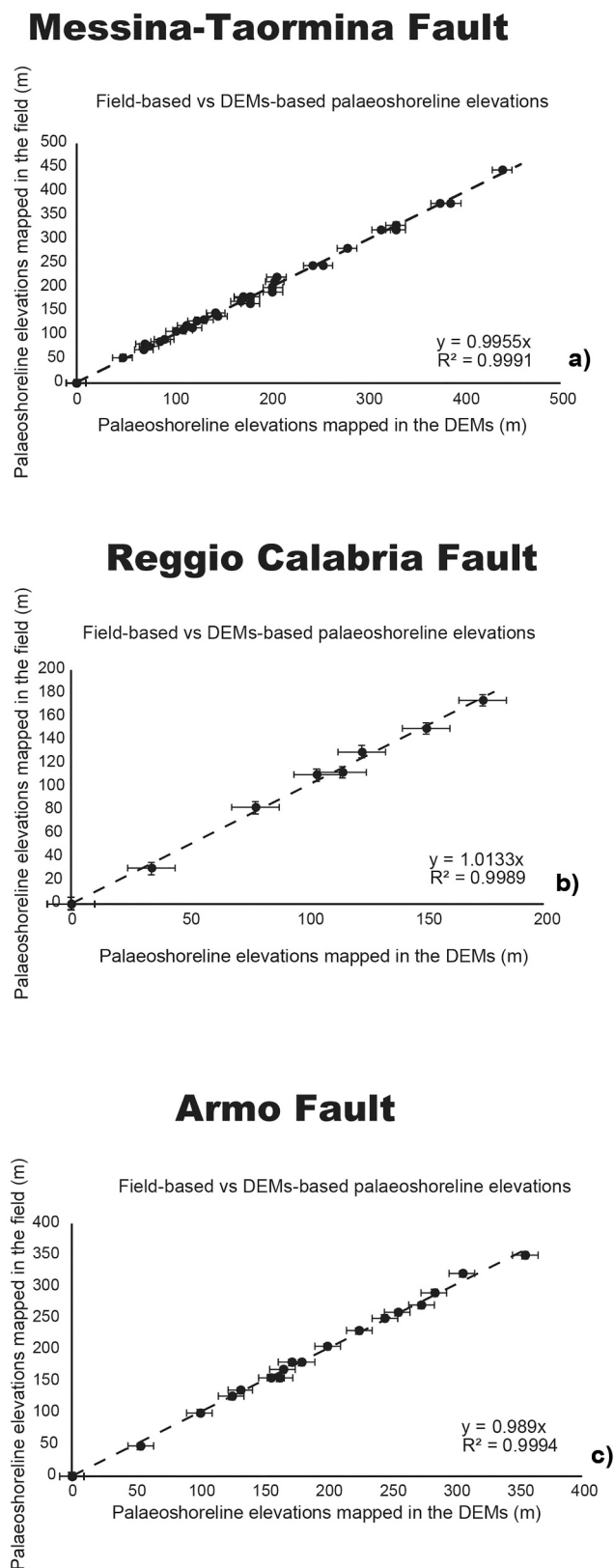
Messina-Taormina Fault

Field-based vs DEMs-based palaeoshoreline elevations

$$y = 0.9955x$$
$$R^2 = 0.9991$$

a)

Reggio Calabria Fault

Field-based vs DEMs-based palaeoshoreline elevations

$$y = 1.0133x$$
$$R^2 = 0.9989$$

b)

Armo Fault

Field-based vs DEMs-based palaeoshoreline elevations

$$y = 0.989x$$
$$R^2 = 0.9994$$

c)

Fig. 4. Linear regression analysis showing the relationship between field-based and DEM-based inner edge elevation measurements for the Messina-Taormina Fault (a), Reggio Calabria Fault (b) and Armo Fault (c). The R^2 value >0.99 confirms a strong correlation suggesting that elevations measured from the DEM are likely to be accurate.

(~125 ka) is at ~220 m near Nizza di Sicilia whereas we suggest this palaeoshoreline (125 ka – MIS 5e) is at ~170 m elevation (topographic profiles 8 and 9 show the palaeoshoreline elevation between 160 m and 173 m), defining an amplitude of uplift-variation along strike that is bigger than in our interpretation. Moreover, we show that in most cases prominent palaeoshorelines on the sea level curve, mapped elsewhere in the Mediterranean realm such as the 125 ka (MIS 5e), 240 (MIS 7e) and the 340 ka (MIS 9e) (e.g. Cerrone et al., 2021b; Meschis et al., 2020; Roberts et al., 2013; Robertson et al., 2019), identify clear geomorphic inner edges of marine terraces on topographic profiles. More subtle sea level highstands such as the 76.5 ka (MIS 5a) as recognized by others in northern Calabria (Cerrone et al., 2021a), the second peak of the MIS 5e (119 ka) already recognized in SE Sicily (Meschis et al., 2020) and Apulia region (De Santis et al., 2021) within the Italian territory, and the 410 ka (MIS 11c) are also identified in places across all the 3 faults (in total, we identify palaeoshorelines from 50, 76, 100, 125, 200, 240, 310, 340, 410, 478 ka).

In our interpretation, values of uplift rates in the footwall of the Messina-Taormina Fault vary from ~0.5 mm/yr close to the NNE tip zone to ~0.8 mm/yr in the centre of the fault pre- 50 ka; post- 50 ka uplift rates accelerated from ~1.2 mm/yr close to the NNE tip zone to ~1.9 mm/yr in the centre of the fault (Fig. 6d); this implies an uplift rate increase through time by a factor in the range of 2.375–2.400 (Table 4a). For the hangingwall of the Reggio-Calabria Fault, values for uplift rates for pre-50 ka are 0.9 mm/yr beyond the NNE tip zone and 0.55 mm/yr close to the centre of the fault, with accelerated uplift-rate values after 50 ka of 2 mm/yr beyond the tip zone and 1.33 mm/yr close to the centre of the fault (Fig. 6e); this indicates an uplift-rate increase by a factor in the range of 2.222–2.418 (Table 4a). It is important to note that close to the Scilla region, our uplift rates from Profile 14 for the post-50 ka (2 mm/yr) are in agreement with Late Holocene uplift rates (~2 mm/yr) proposed by others (Antonioli et al., 2006a; Antonioli et al., 2021; Ferranti et al., 2007). For the hangingwall of the Armo Fault, uplift-rates vary between 0.85 mm/yr close to the southern tip and 0.56 mm/yr close to the centre of the fault prior to ~50 ka, with accelerated uplift rate values after 50 ka of 2.2 mm/yr close to the southern tip and 1.45 mm/yr close to the centre of the fault (Fig. 6f); this indicates an uplift-rate increase by a factor in the range of 2.588–2.589 (Table 4a). In summary, the range of uplift-rate increase factors from these 6 different locations (3 fault centres and close to 3 fault tips) is small (2.222–2.589), with an average value of 2.43. This small range, and the fact that all 6 values were derived from independent calculations, suggests this is unlikely to be due to chance, but rather reflects a real change in the distribution of strain that affects all 3 faults in a similar manner. We discuss this further below, but here note that change in fault-controlled uplift rates over the Late Quaternary are not unprecedented; for instance, within the Gulf of Corinth in Greece, tectonically deformed palaeoshorelines mapped within the footwall of the South Alkyonides Fault indicate that uplift rates have varied through time, with an uplift-rate change factor of ~3.20 at ~175 ka, suggesting an acceleration of slip-rate for this normal fault (Roberts et al., 2009).

We calculate how much the mapped palaeoshorelines have been tilted along-strike due to displacement gradients along the fault. This tests the hypothesis that the faults have been active throughout the Late Quaternary, because if this is the case older palaeoshorelines will have experienced a longer history of deformation and hence should exhibit higher tilt angles (e.g. Armijo et al., 1996; Meschis et al., 2018; Roberts et al., 2013; Robertson et al., 2019). Results confirm that the topographically higher and older palaeoshorelines present higher tilt angle values, demonstrating that they have experienced a longer faulting history, with progressive active faulting throughout the Middle-Late Pleistocene (Fig. 7). It is important to note that similar along-strike variations of Late Holocene uplift, associated rates and tilting over 10 km along the strike of the Messina-Taormina Fault, close to its southern tip, had been reported by previous studies, suggesting faulting activity (Antonioli et al., 2006a; De Guidi et al., 2003; Spampinato et al., 2012),
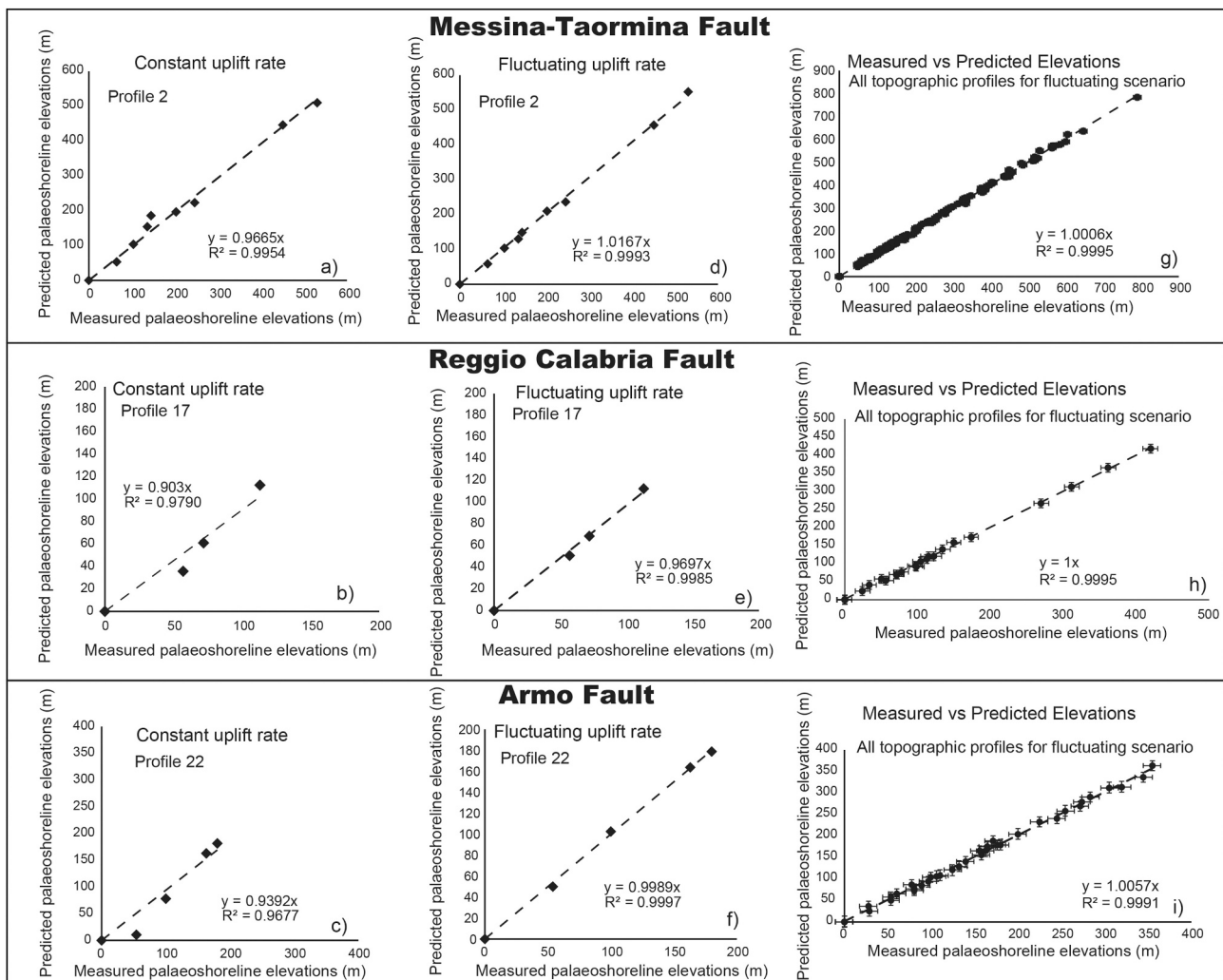
Fig. 5. Linear regression analysis for all 3 investigated faults showing that a better and higher R^2 value is obtained if a changing uplift rate through time is claimed to model multiple mapped palaeoshoreline elevations and multiple synchronously-predicted sea-level highstand elevations. Indeed, constant scenario (a, b and c) vs fluctuating scenario (d, e and f) for one topographic profile for each fault is shown. Linear regression for all topographic profiles (1–22) for the fluctuating scenario are shown in g, h and i. Linear regression analysis between our measured and predicted palaeoshoreline elevations for the Messina-Taormina Fault, Armo Fault and Reggio Calabria Fault for each topographic profile (1–22) is shown in Fig. SM 11–18. The predicted elevations, representing the synchronously calculated sea-level highstand elevations, indicate a fluctuating uplift rate through time, that has been derived by iterating uplift rates to find the best match to the measured and mapped palaeoshorelines. Note that "measured" elevations represent palaeoshoreline elevations mapped in the 10 m high resolution DEMs. Coefficient of determination, R^2 value, has been used between these two datasets to quantify the best fit for all topographic profiles presented in this paper, with a value >0.99.

so our result is consistent with theirs.

To gain information on fault slip-rates from uplift-rates it is important to note that the acceleration in uplift at ~50 ka, measured on (i) hangingwalls of Reggio Calabria Fault and Armo Fault and (ii) footwall of the Messina-Taormina Fault, must reflect the interplay between fault-related vertical motions and vertical motions that are more "regional" in nature either related to the underlying subduction system or mantle upwelling processes through slab window (Gvirtzman and Nur, 1999a; Malinverno and Ryan, 1986; Westaway, 1993). It is widely accepted that there is an important regional uplift in this region, but debate surrounds the precise value, and how it can be separated from more subduction/mantle upwelling-related regional uplift variations produced by normal faulting (e.g. Meschis et al., 2018; Roberts et al., 2013). However, if the regional uplift stayed constant through time, and affects both the hangingwall and footwalls of the active normal faults, then the following is implied: (i) the footwall uplift on the Messina-Taormina Fault has accelerated at ~50 ka, suggesting that the throw-rate on the fault increased at ~50 ka; (ii) the component of hangingwall subsidence produced by slip on the Reggio Calabria Fault and Armo Fault has

decelerated at ~50 ka implying that the throw-rates on these faults decreased at ~50 ka. If our assumption is correct, and regional uplift-rates have remained constant through time, this out-of-phase behaviour, where the slip-rates on some faults accelerate accompanied by a synchronous deceleration of slip on others, implies that some sort of fault interaction may be operating.

4.3. Field observations that help to convert uplift-rates into throw-rates on the faults

We have collected a number of field observations that allow us to convert uplift-rate histories into throw-rate histories on the faults.

The long-term throw-rate on the Reggio Calabria Fault can be constrained because we have observed in the field a mapped faulted-offset of the 125 ka (MIS 5e) marine terrace along the fault-crossing Profile 16. For the hangingwall of the fault, age constraints in the literature (Balescu et al., 1997 - Table 1) driving our synchronous correlation technique suggest that a prominent terrace composed of marine conglomerates dates to the 5e highstand at ~125 ka. These marine
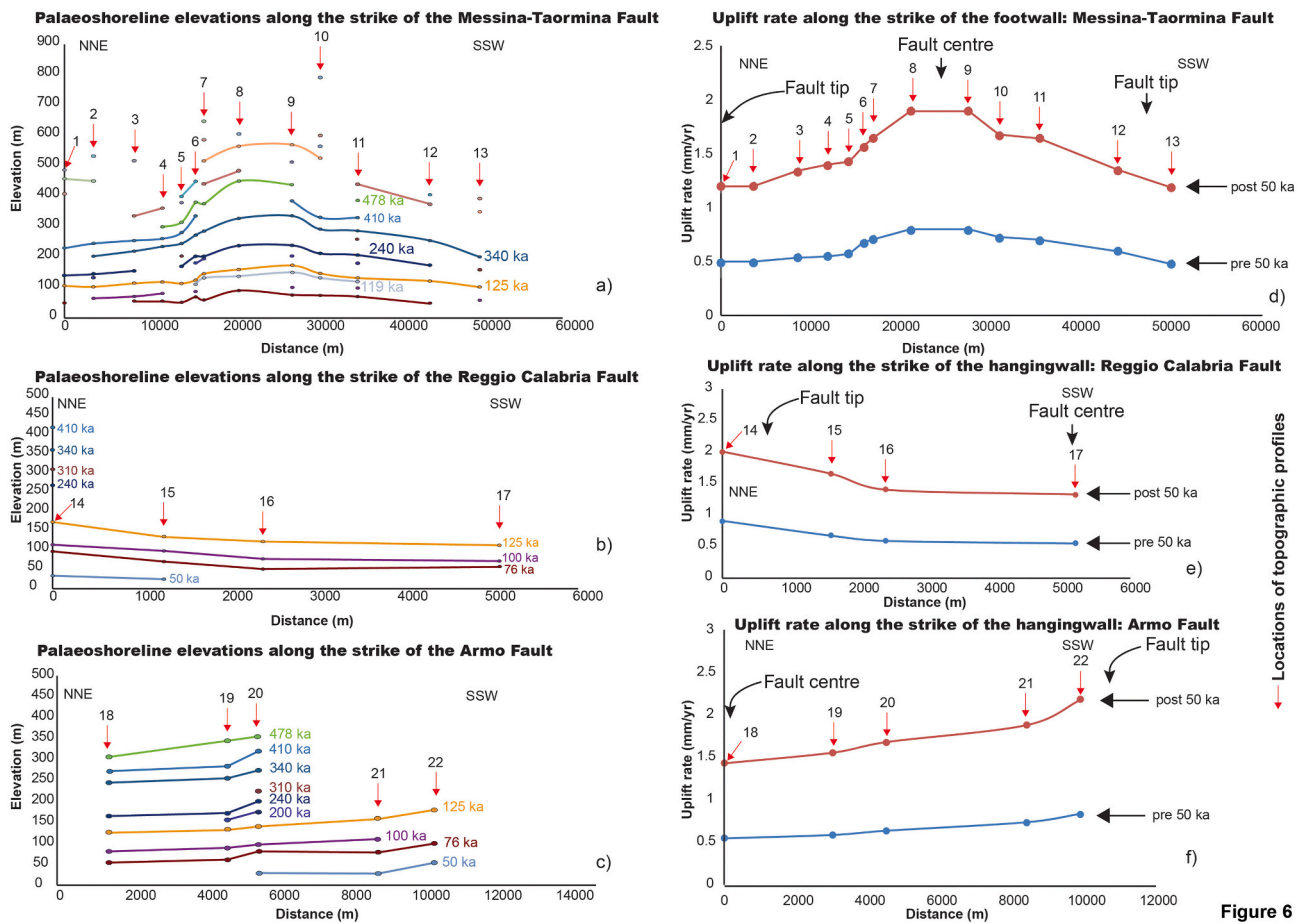
Fig. 6. Crustal uplift and uplift rates over the Quaternary. Topographic profiles from Fig. 1 are labelled. Palaeoshoreline elevations change along the strikes of the Messina-Taormina Fault (a), Reggio Calabria Fault (b) and Armo Fault (c), suggesting Late Quaternary faulting activity. Spatial variations of rates of uplift measured along the strikes of the investigated faults and on the footwall of the Messina-Taormina Fault (d) and on hangingwalls of the Reggio Calabria Fault (e) and the Armo Fault (f). Changes in uplift rates through time ("Pre-50 ka" and "post-50 ka") are shown, derived by applying a synchronous correlation approach on the investigated palaeoshorelines deformed by normal faulting activity.

conglomeratic deposits are associated with the highest terrace surface along the Profile 16 at ~123 m elevation (Fig. 8). On the footwall cut-off a marine conglomerate deposit exists at ~190 m (Fig. 8), which can be mapped up-dip to a prominent terrace surface. Although we have not achieved a direct age determination of the footwall deposits, we have derived ages for material that is contained within the same terrace, and hence pre-dates this conglomerate, sampled at an elevation of 230 m. We achieved ^{234}U/^{230}Th age determinations for a death assemblage of detrital corals contained within a boulder of cemented shallow marine sands in this conglomerate of 449 ± 17 ka, 384 ± 11 ka and 480 ± 25 ka (Table 2). These ages suggest a minimum age of formation of this boulder of 384 ± 11.5 ka (implying the 448 ± 17 ka and 480 ± 25 ka corals are detrital ages for corals inherited from a previous highstand at 384 ± 11 ka). However, the boulder itself is detrital, and its age should be older than the terrace deposits within which it is found. Thus, 384 ± 11 ka is the maximum age of the marine terrace deposit containing the boulder, and the actual age must be younger. It is suggested its age is 125 ka because a very lithologically similar layer of marine conglomerate that caps the marine terrace related to the 125 ka highstand (Balescu et al., 1997; Catalano et al., 2003), has been mapped on the hangingwall of the same fault with a base at ~123 m. If the terraces are one and the same, this implies a vertical offset across the fault of ~77 m over 125 ka (Fig. 8). Note that this throw is derived by looking at the same faulted marine conglomeratic deposits in the hangingwall and footwall cut-offs. This would suggest a long-term fault throw-rate averaged over 125 kyrs of 0.62 ± 0.04 mm/yr, in agreement with

previous studies which have used offsets of Tyrrhenian deposits and the height of triangular facets (0.6 mm/yr - Monaco and Tortorici, 2000). However, the interpreted increase in uplift-rate in the hangingwall at ~50 ka means that the 125 kyrs average throw-rate should not be used over shorter time intervals. If the uplift-rate change factor is applied (2.43) for the ~77 m of mapped vertical offset (Fig. 8), the throw-rate was 0.80 mm/yr from 125 ka to 50 ka and 0.33 mm/yr from 50 ka to the present day, implying that the throw-rate decreased by a factor 0.41 at ~50 ka (Fig. 8 and Table SM 2 for throw calculations).

For the Armo Fault, its long-term throw rate can be constrained due to the mapped offset of a marine terrace associated to the 478 ka sea level highstand, a refined age derived by applying a synchronous correlation approach along the fault-crossing Profile 20 (Figs. 9 and 1 for profile location). In particular, we show that the topographically highest and oldest terrace mapped on the hanging wall of the Armo Fault at 355 m dates from 478 ka, according to our synchronous correlations. This terrace, as well as all the lower terraces mapped along the Profile 20 (Fig. 9), is cut into Plio-Pleistocene bioclastic and siliciclastic marine sandy deposits (Chiarella et al., 2021). A flat terraced surface at the footwall cut-off of the Armo Fault is mapped at ~700 m cut into the Palaeozoic rocks. If this footwall terrace is assumed to be coeval and with the same age of the hangingwall cut-off terrace mapped at 355 m with a synchronously-derived age of 478 ka, this implies a vertical displacement of 345 m, suggesting a throw-rate of 0.72 ± 0.012 mm/yr averaged over 478 kyrs in agreement with other geoscientists that have independently studied this fault through geomorphological

Table 4
Uplift-rate change factors (a) and uplift-rate-derived throw-rate change factor (b) are shown. Note that acceleration of uplift rates is mapped on both coastlines of the Messina Strait.

a)

Fault	Before 50 ka (mm/yr) – Uplift Rate 1 (UR1)	After 50 ka (mm/yr) – Uplift Rate 2 (UR2)	Range of uplift-rate change factor – UR2/UR1
Messina-Taormina (footwall)	0.5–0.8	1.2–1.9	2.375–2.400
Reggio Calabria (hangingwall)	0.55–0.9	1.33–2	2.222–2.418
Armo (hangingwall)	0.56–0.85	1.45–2.2	2.589–2.588

b)

Fault	Before 50 ka (mm/yr) – throw rate 1 (TR1)	After 50 ka (mm/yr) – throw rate 2 (TR2)	Uplift-rate-derived throw rate change factor – TR2/TR1
Messina-Taormina	0.96	2.34	2.43
Reggio Calabria	0.81	0.33	0.41
Armo	0.77	0.32	0.41

investigations (e.g. 0.7 mm/yr - Roda-Boluda and Whittaker, 2017). However, the interpreted decrease in throw-rate at ~50 ka from uplift rates suggests that the 478 kyrs average throw-rate should not be used over shorter temporal windows. If the uplift-rate change factor is applied (2.43) then from 478 ka to 50 ka the throw-rate was 0.77 mm/yr and from 50 ka to present day 0.32 mm/yr for 345 m of offset, implying that the throw-rate decreased by a factor 0.41 at ~50 ka in the hangingwall (Fig. 9 and Table SM 2 for throw calculations).

For the Messina-Taormina Fault, we do not have direct measurements of faulted offsets of Late Quaternary deposits. However, we derive a throw-rate by subtracting the rate of regional uplift and utilising a value for the ratio of footwall uplift and hangingwall subsidence. In particular, we map the highest uplift rates of 1.9 mm/yr (50 ka to present) in centre of the fault along Profiles 8 and 9 (Fig. 6d). Previous studies have suggested that a "regional" component of uplift, with a rate of ~1 mm/yr for this region (Ferranti et al., 2007; Spampinato et al., 2014; Westaway, 1993), and our observations close to the fault tip, where the effect of faulting would be minimised, approach this value, supporting the ~1 mm/yr "regional" uplift rate. For these reasons, we subtract 1 mm/yr from the "total" mapped post-50 ka uplift rate in the centre of the fault of 1.9 mm/yr (1.9–1 mm/yr = 0.9 mm/yr of footwall uplift) and we then apply a uplift/subsidence ratio of 1:1.6, a value proposed for active normal faults within the Calabrian Arc by previous studies (Quye-sawyer et al., 2021). This implies a hangingwall subsidence of 1.44 mm/yr that, if summed with 0.9 mm/yr of footwall uplift, implies a throw-rate of 2.34 mm/yr for the last 50 kyrs (0.9 mm/yr footwall uplift plus 1.44 mm/yr hangingwall subsidence). If the uplift rate change factor is applied (2.43), then a throw-rate of 0.96 mm/yr before 50 ka is suggested.

5. Discussion

As observed herein and worldwide within zones of convergence such as active subduction zones, uplifted palaeoshorelines can be used to derive rates of crustal deformation through time, from seismically deforming upper plates (e.g. Catalano et al., 2003; Catalano and De Guidi, 2003; De Guidi et al., 2002; González-Alfaro et al., 2018; Ott et al., 2019; Roberts et al., 2009; Roberts et al., 2013; Robertson et al., 2019; Saillard et al., 2009; Shikakura, 2014; Shyu et al., 2018).

For Calabria, Quye-Sawyer et al. (2021) and Roda-Boluda and

Whittaker (2017) suggest an increase in throw-rate on the Serre, East Crati and Cittanova faults (Fig. 1) between ~100–300 ka, using observations of knickpoints along rivers crossing these faults and incising into marine terraces, attributing these changes to the interaction of these faults during fault growth and linkage. The questions that arise are (a) whether these slip-rate changes are related to a change in rate across the whole subduction system or due to a change in the internal organisation of strain of the upper plate of the subduction system, and (b) how the changes in rate influence seismic hazard. We discuss a comparison between the rates we have measured, and regional extension rates measured with GPS and then discuss seismic hazard (Fig. 10).

5.1. The relationship between fluctuating slip-rates on individual faults and the regional extension rate

Constraints on the regional extension rate are available from GPS observations and modelling based on those observations. Serpelloni et al. (2010) observed a maximum extensional strain-rate of ~65 nanostrains/yr and an extension rate of 3 mm/yr across the Messina Strait (Fig. 10). Inversion of these observations is attempted to resolve slip-rate on faults and the bootstrap analysis of model uncertainties. It shows that for a modelled fault that "dips gently SE-ward" located in the Messina Strait with dimensions and location similar to the Messina-Taormina fault considered herein, optimal values of $3.5 + 2.0/-1.3$ and $1.6 + 0.3/-0.2$ mm/yr for the dip–slip and strike–slip components are found, respectively, locked above $7.6 + 4.6/-2.9$ km depth. We show the implied heave-rate through time for these inversion results as an inset in Fig. 10d.

In order to compare our results with those from Serpelloni et al. (2010), we have summed the implied throw-rates on the faults through time and converted these into heave-rates (extension rates) by assuming fault dips ranging from 40 to 70° (Fig. 10d and Table SM 3 for calculations). Although the throw-rates on the faults decrease at 50 ka by a factor of 0.41 on the Reggio Calabria Fault and on the Armo Fault, alongside an increase by a factor of 2.43 at 50 ka on Messina-Taormina Fault, the combined effect of these out-of-phase throw-rate histories is to maintain a relatively constant heave-rate (see before and after the red dashed line in Fig. 10d). These results are not inconsistent with those from Serpelloni et al. (2010), although we prefer higher values for fault dip constrained with field measurement from outcropping fault planes for the Armo and Reggio-Calbaria faults, and modelling of coseismic effects from the 1908 earthquake (Meschis et al., 2019). This suggests that these slip-rate changes are not related to a change in rate across the whole subduction system, but rather due to a change in the internal organisation of strain of the upper plate of the subduction system. It is worth noting that these faults are closely spaced across-strike, with a distance <10–15 km at the base of the seismogenic layer, where large earthquakes likely nucleate. This distance is much less than half a fault length (~29 km for the Messina-Taormina Fault which is 58 km in length), a distance within fault interaction is expected. This is consistent with the conclusions from Quye-Sawyer et al. (2021) and Roda-Boluda and Whittaker (2017) who suggest that slip-rate changes in Calabria in the Late Quaternary are due to interactions between faults. Where one fault increases its slip-rate other faults across strike decrease their slip-rates to maintain constant regional strain-rates, and this has been reported in a number of other locations (the North Sea, central Italy, central Greece, Baja California, New Zealand; (Cowie et al., 2005, 2017; Cowie and Roberts, 2001; Gupta et al., 1998; Nicol et al., 2006; Roberts et al., 2002; Roberts and Michetti, 2004), and in models of activity rates on faults (Cowie et al., 2012; Cowie, 1998; Cowie and Roberts, 2001; Mildon et al., 2019; Sgambato et al., 2020).

Our observations suggest summed heave-rates in the range of 0.92–3.56 mm/yr across faults that are assumed to dip in the range of 40-70°, but note that in detail it is challenging to reconcile this with the heave rates of 0.75–4.76 mm/yr derived through inversion of GPS data by Serpelloni et al. (2010) because they suggest a $30 + 1.1/-0.7°$ SE-
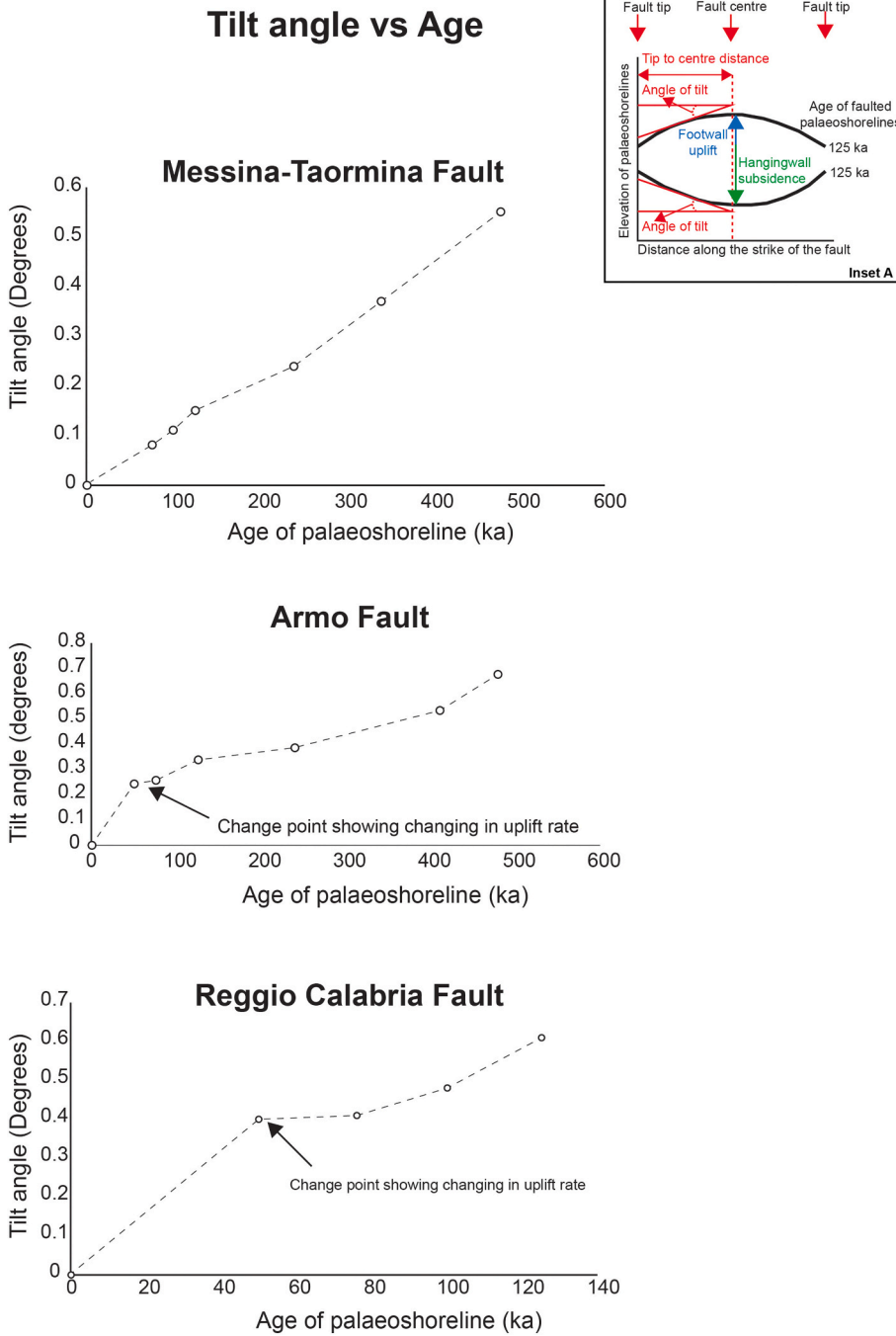
Fig. 7. Tilt angle values calculated for each mapped palaeoshoreline shown in Fig. 6a–c, showing that older palaeoshorelines have higher tilt angles, suggesting that they have experienced a longer history of differential uplift, and that differential uplift has been ongoing progressively during the Late Quaternary. Note that for the Messina-Taormina Fault, a flex point is not recorded because we were not able to map palaeoshorelines belonging to the 50 ka sea level highstand. Inset A shows a no-scaled cartoon sketch of the tilt angle of a palaeoshoreline along the strike of a fault.

Note that values of tilt angle for each investigated palaeoshoreline have been calculated as a $\tan^{-1}$ of a gradient "m" of a straight-line equation (y = mx), as proposed by previous studies (Meschis et al., 2018; Meschis et al., 2020; Robertson et al., 2019).

ward dipping normal fault. It is challenging because Meschis et al. (2019) show that a dip of ~70° for the Messina-Taormina Fault is required to explain levelling data of the coastline that was deformed by the 1908 Mw 7.1 Messina earthquake, not 30 + 1.1/−0.7° implied by the results of Serpelloni et al. (2010). Possible explanations of this disparity are unclear, but may include factors such as (a) that Serpelloni et al. (2010) only included a single fault in their inversion, whilst the palaeoshoreline data we present show that at least 3 faults have been active during the Late Quaternary, (b) that rates measured over interseismic timescales where elastic processes dominate (e.g. decadal timescales from GPS), may differ from rates measured over multiple seismic cycles (10^4–10^5 year timescales from deformed Quaternary palaeoshorelines) and (c) that the nearby Mt. Etna volcano has undergone changes in its chemistry due to re-organisation of the volcanic

plumbing system in the Late Quaternary (plume–arc transition recorded by Etnean primitive melt inclusions from 125 ka – to present; Schiano et al., 2001), or even at ~60 ka (Barreca et al., 2018), and these changes may be associated with changes in the spatial distribution of strain within the overall subduction system. More work is needed to reconcile rates measured over different timescales. Serpelloni et al. (2010) do show that changes in slip-rate of several millimetres per year can be produced by changes in the locking depths of faults in the overall subduction system, and hence how faults interact, and this may be a way forward towards reconciling slip-rates measured over different timescales. However, for now we conclude that the changes in slip-rates we have constrained are broadly consistent with those in Serpelloni et al. (2010), but our results suggest that rates of late Quaternary slip appear to have been out-of-phase on faults located across strike from each other,
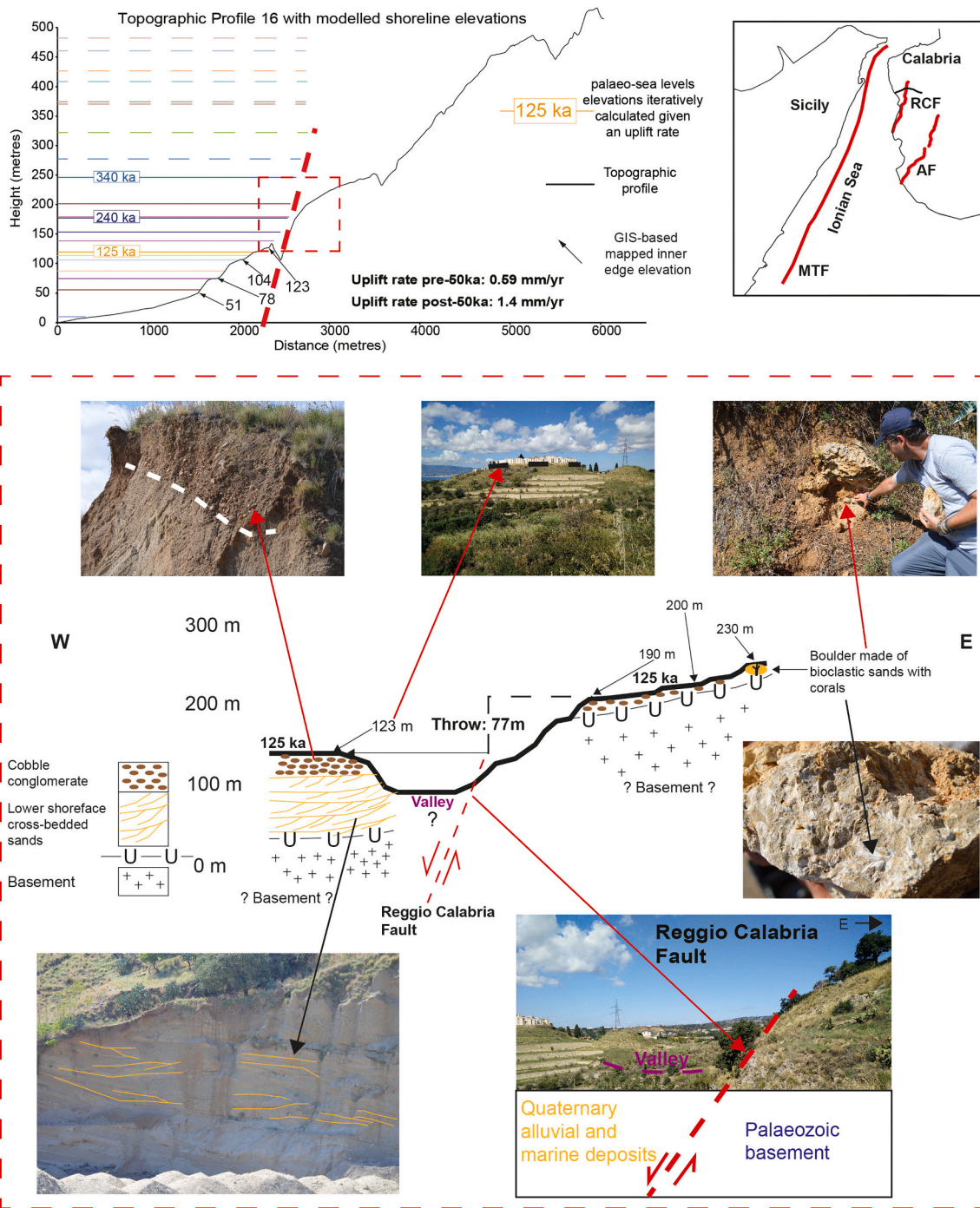
Fig. 8. Cartoon field sketch showing the Reggio Calabria Fault offsetting terraced shallow marine deposits over 125 ka. On the footwall terrace a boulder made of cemented bioclastic sands containing corals with ages given in Table 2 (Samples 15, 16 and 17) and the significance of the ages described in the text. Note that elevations of the same marine conglomeratic deposits are mapped in the hangingwall cut-off and footwall cut-off, implying a throw of 77 m.

and the summed heave rate is relatively constant through time, suggesting that the slip-rate changes are not related to a change in rate across the whole subduction system, but instead due to a change in the internal organisation of strain of the upper plate of the subduction system. Finally, we speculate, that this apparent decoupling between subduction rates and slip rates on faults in the upper plate may have implications in terms of maximum magnitude for shallow crustal compressional earthquakes along the Ionian subduction zone. Based on the Italian seismic catalogue, likely the most complete catalogue worldwide, we have no record of strong subduction earthquakes in the Calabrian arc (e.g. Maesano et al., 2017; Sgroi et al., 2021). Ionian

subduction is relatively aseismic at least in the first 30–60 km. This fits very well with the seismotectonic interpretations proposed in the literature (e.g. Gvirtzman and Nur, 1999a, 1999b), showing that the asthenosphere is shallow and just beneath the Calabrian arc; and describing thermal conditions in the crust so that the coupling between the subducting plate and the Calabrian arc is very poor. We speculate that this puts a limit (Mw ca. 6.0) to the maximum compressive earthquake that can occur in the shallow crust (first 30–60 km) of the Calabrian arc. In this scenario, strong shallow crustal earthquakes are limited to the upper plate, while aseismic creep dominates along the subduction interface. We finally stress that our study suggests that more
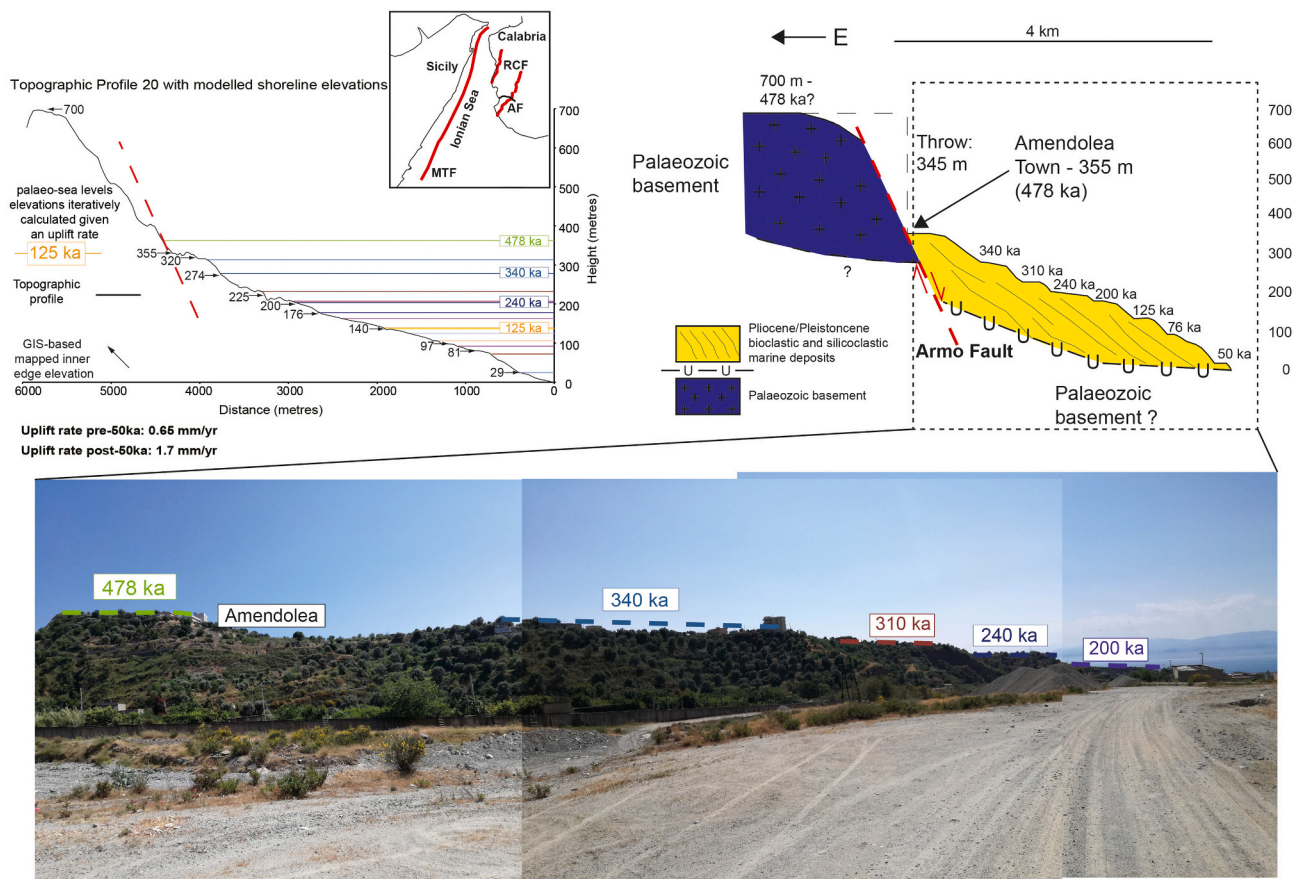
Fig. 9. Topographic profile and field sketch showing mapped uplifted palaeoshorelines on the hangingwall of the Armo Fault cut into Plio-Pleistocene marine deposits. It is also shown the Armo Fault offsetting the synchronously-derived 478-aged marine terrace, suggesting faulting activity over the Late Quaternary. Bottom photo shows some of the palaeoshorelines mapped on the hangingwall of the Armo Fault along the Profile 20. Profile location is shown in Fig. 1.

investigations are needed, combining geodetic and geologic measurements, to better refine rates of crustal deformation within upper plates above subduction zones at different timescales.

5.2. Fault interaction and its impact on seismic hazard assessment within the Messina Strait

In relation to the seismic hazard affecting the Messina Strait, the newly-refined long-term fault throw-rates in this paper, and the associated T_{mean} values (or also known as Earthquake Recurrence Interval), play a crucial role for seismic hazard calculations. For example, Earthquake Recurrence Intervals (or T_{mean}) for a given earthquake magnitude are shorter for higher fault slip-rates (e.g. Cowie and Roberts, 2001). We are aware that in some cases rates of deformation are averaged over longer and different timescales (e.g. Martín-Banda et al., 2021; Roberts et al., 2013; Robertson et al., 2019) compared to this study because it is simply difficult to obtain more detailed faulting activity through time. However, herein, using a throw-rate on the Reggio Calabria Fault for instance over 125 kyr would provide a misleadingly short value for T_{mean}. This is because the throw-rate decreased by a factor of 0.41 at 50 ka (throw-rate over 125 ka = 0.62 mm/yr; assuming 1 m slip per event implies a T_{mean} of 1612 years; throw-rate over 50 ka = 0.33 mm/yr; assuming 1 m slip per event implies a T_{mean} of 3030 years). Similarly, for the Armo Fault, whose throw-rate has decreased by a factor of 0.41 at 50 ka (throw-rate of 0.32 mm/yr), this would imply a T_{mean} of 3125 years assuming a 1 m slip per event, rather than a T_{mean} of 1388 years for throw-rate of 0.72 mm/yr over the last 478 kyrs. For the Messina-Taormina Fault, we estimate a T_{mean} of 427 years assuming 1 m slip per event or 855 years assuming 2 mm slip per event for a throw-rate of

2.34 mm/yr over the last 50 ka. These values are summarized in Table 5. Thus, in this paper, we emphasise that it is vital to assess not just the throw-rate, but also the variability in throw-rates through time on a fault so that an appropriate throw-rate can be used in seismic hazard calculations. However, to do this, one must identify the correct ages of geological markers used in defining slip-rates.

Overall, our results produce a pattern of uplift through time that differs from previous authors (e.g. Catalano et al., 2003; Catalano and De Guidi, 2003; De Guidi et al., 2002; Pavano et al., 2016). In particular, our interpretations suggest a major re-organisation of the activity rates on the three main faults in the region at ~50 ka that has not been noted by previous authors. Changes in activity rate have been reported from further north on the Cittanova, Serre and East Crati faults (Quye-Sawyer et al., 2021; Roda-Boluda and Whittaker, 2017). Finally, it is important to note that recently authors have claimed a possible different seismogenic source from the Messina-Taormina Fault for the 1908 Messina Earthquake (Barreca et al., 2021). In particular, they propose an offshore NNE-oriented fault, named "W-Fault", with its onshore prolongation bending towards southern Calabria, for a total length of ~34 km (Fig. 15 from Barreca et al., 2021), close to our Profiles 14 and 15 on the hangingwall of the Reggio Calabria Fault. However, note that this geometry and orientation would not explain the geomorphology of well-mapped and tectonically deformed marine terraces in this paper and by others on the footwall of the Messina-Taormina Fault. Indeed, where lower uplift rates are mapped close to Messina town in this paper and already proposed in other studies (e.g. Catalano and De Guidi, 2003; Pavano et al., 2016) coincides with the centre of the "W-Fault" proposed by Barreca et al., 2021, and thus where a maximum long-term footwall-related uplift rate should be expected. Furthermore, on its onshore
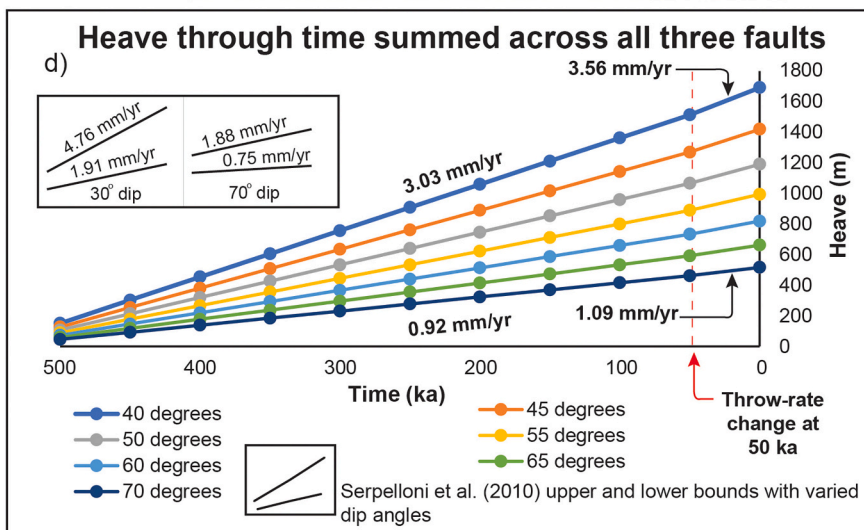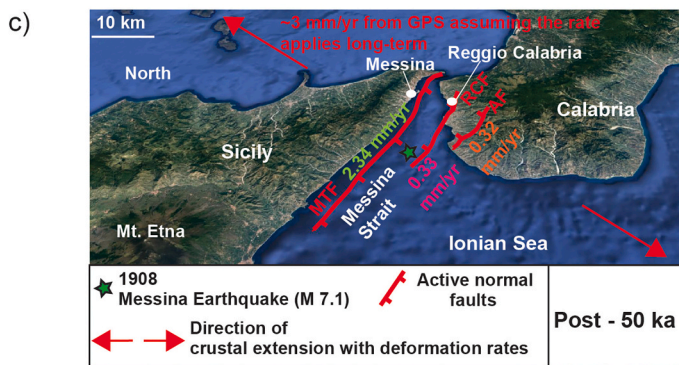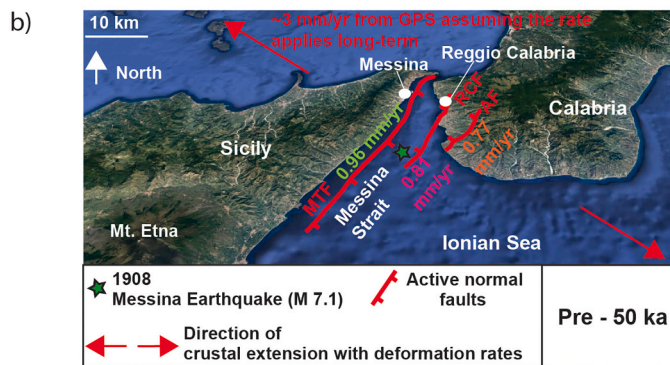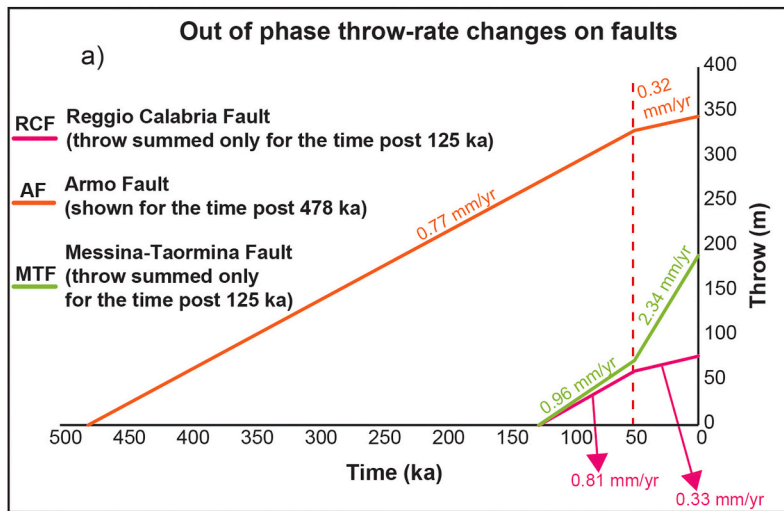
Fig. 10. (a) Throw-rates through time are shown for the Messina-Taormina Fault, Reggio Calabria Fault and Armo Fault. Changing throw rates through time have been calculated from faulted coeval marine terraces for the Reggio Calabria Fault and Armo Fault. In (b) and (c) a tectonic sketch with refined throw-rate through time, pre and post 50 ka, with horizontal extension rates from Serpelloni et al. (2010). Note that photos are from Google EarthTM (Maxar Technologies, Landsat). In (d), values of throw-rates-converted heave rates are shown, iterating different fault dip-angles for all 3 investigated faults, compared to those proposed by Serpelloni et al. (2010) using geodetic measurements. In (d), we assume that fault dip angles for all 3 investigated faults are the same because we have no information for those values.

The contrast of changing throw-rates of individual faults with constant heave-rates when summed all the faults suggests that faults are interacting to maintain the regional extension rate.

Table 5

Values of Earthquake Recurrence Interval (T_{mean}) are summarized showing the variability if pre-50 ka rates and/or long-term rates are used instead of post-50 ka rates. Note that throw-rates for the Messina-Taormina Fault are for the first time estimated in this paper, implying that no long-term rates are available from literature.

Fault name (slip per event in m)	T_{mean} using 125 ka long-term throw-rate (years)	T_{mean} using pre-50 ka throw-rate (years)	T_{mean} using post-50 ka throw-rate (years)
Messina-Taormina (1 m slip)	–	1042	427
Messina-Taormina (2 m slip)	–	2083	855
Reggio Calabria (1 m slip)	1612	1234	3030
Armo (1 m slip)	1388	1299	3125

prolongation there is no either co-seismic evidence or mapped fault scarp likely produced by successive earthquakes; instead, the Reggio Calabria Fault is well-known and previously mapped by several studies (Aloisi et al., 2013; Basili et al., 2008; INGV - DISS Working Group, 2018; Monaco and Tortorici, 2000), deforming the marine terraces outcropping along the Calabrian coastline of the Strait.

6. Conclusion

A new uplift rate scenario has been presented within the tectonically extending Messina Strait, southern Italy, on the upper plate of the Ionian Subduction zone by refining ages of tectonically deformed Late Quaternary marine terraces. Palaeoshorelines investigated on the Sicilian coast, lying on the footwall of the offshore Messina-Taormina Fault, show along-strike deformed geometry, implying faulting activity over the Late Quaternary. Similarly, long-term faulting activity is implied for the Reggio Calabria Fault and the Armo Fault by showing along-strike deformed geometries of palaeoshorelines. Changes of uplift rates along-strike of the investigated faults confirm: (i) tectonic subsidence of the hangingwalls, which is presumably counteracting the "regional" uplift signal possibly associated either with the Ionian subduction process (Malinverno and Ryan, 1986; Roberts et al., 2013) or with mantle upwelling (Gvirtzman and Nur, 1999b), and (ii) the footwall tectonic uplift. The changes in uplift rates are determined to be correlated with some faults speeding up and others slowing down at around 50 ka. We stress that this new scenario of temporally changing fault throw-rates has critical tectonic implications and effect the long-term seismic hazard approach either for the Messina Strait region and worldwide.

Supplementary data to this article can be found online at https://doi.org/10.1016/j.geomorph.2022.108432.

Declaration of competing interest

The authors declare that they have no known competing financial interests or personal relationships that could have appeared to influence the work reported in this paper.

Data availability

Data will be made available on request.

References

Aloisi, M., Bruno, V., Cannavò, F., Ferranti, L., Mattia, M., Monaco, C., Palano, M., 2013. Are the source models of the M 7.1 1908 Messina Straits earthquake reliable? Insights from a novel inversion and a sensitivity analysis of levelling data. Geophys. J. Int. 192, 1025–1041. https://doi.org/10.1093/gji/ggs062.

Anders, M.H., Schlische, R.W., 1989. Overlapping faults, intrabasin highs, and the growth of normal faults. J. Geol. 102.

Antonioli, F., Calcagnile, L., Ferranti, L., Mastronuzzi, G., Monaco, C., Orrù, P., Quarta, G., Pepe, F., Scardino, G., Scicchitano, G., Stocchi, P., Taviani, M., 2021. New evidence of MIS 3 relative sea level changes from the Messina Strait, Calabria (Italy). Water 13, 2647. https://doi.org/10.3390/w13192647.

Antonioli, F., Ferranti, L., Lambeck, K., Kershaw, S., Verrubbi, V., Dai Pra, G., 2006a. Late Pleistocene to Holocene record of changing uplift rates in southern Calabria and northeastern Sicily (southern Italy, Central Mediterranean Sea). Tectonophysics 422, 23–40. https://doi.org/10.1016/j.tecto.2006.05.003.

Antonioli, F., Kershaw, S., Renda, P., Rust, D., Belluomini, G., Cerasoli, M., Radtke, U., Silenzi, S., 2006b. Elevation of the last interglacial highstand in Sicily (Italy): a benchmark of coastal tectonics. Quat. Int. 145–146, 3–18. https://doi.org/10.1016/j.quaint.2005.07.002.

Argnani, A., Brancolini, G., Bonazzi, C., Rovere, M., Accaino, F., Zgur, F., Lodolo, E., 2009. The results of the Taormina 2006 seismic survey: possible implications for active tectonics in the Messina Straits. Tectonophysics 476, 159–169. https://doi.org/10.1016/j.tecto.2008.10.029.

Armijo, R., Meyer, B., King, G.C.P., Rigo, A., Papanastassiou, D., 1996. Quaternary evolution of the Corinth Rift and its implications for the late Cenozoic evolution of the Aegean. Geophys. J. Int. 126, 11–53. https://doi.org/10.1111/j.1365-246X.1996.tb05264.x.

Balescu, S., Dumas, B., Guérémy, P., Lamothe, M., Lhénaff, R., Raffy, J., 1997. Thermoluminescence dating tests of Pleistocene sediments from uplifted marine shorelines along the southwest coastline of the Calabrian Peninsula (southern Italy). Palaeogeogr. Palaeoclimatol. Palaeoecol. 130, 25–41. https://doi.org/10.1016/S0031-0182(96)00119-8.

Barreca, G., Branca, S., Monaco, C., 2018. Three-dimensional modeling of Mount Etna Volcano: volume assessment, trend of eruption rates, and geodynamic significance. Tectonics 37, 842–857. https://doi.org/10.1002/2017TC004851.

Barreca, G., Gross, F., Scarfì, L., Aloisi, M., Monaco, C., Krastel, S., 2021. The Strait of Messina: seismotectonics and the source of the 1908 earthquake. Earth Sci. Rev. 218, 103685 https://doi.org/10.1016/j.earscirev.2021.103685.

Basili, R., Valensise, G., Vannoli, P., Burrato, P., Fracassi, U., Mariano, S., Tiberti, M.M., Boschi, E., 2008. The Database of Individual Seismogenic Sources (DISS), version 3: summarizing 20 years of research on Italy's earthquake geology. Tectonophysics 453, 20–43. https://doi.org/10.1016/j.tecto.2007.04.014.

Catalano, S., De Guidi, G., 2003. Late Quaternary uplift of northeastern Sicily: relation with the active normal faulting deformation. J. Geodyn. 36, 445–467. https://doi.org/10.1016/S0264-3707(02)00035-2.

Catalano, S., De Guidi, G., Monaco, C., Tortorici, G., Tortorici, L., 2003. Long-term behaviour of the late Quaternary normal faults in the Straits of Messina area (Calabrian arc): structural and morphological constraints. Quat. Int. 101–102, 81–91. https://doi.org/10.1016/S1040-6182(02)00091-5.

Cerrone, C., Ascione, A., Robustelli, G., Tuccimei, P., Soligo, M., Balassone, G., Mormone, A., 2021a. Late Quaternary uplift and sea level fluctuations along the Tyrrhenian margin of Basilicata - northern Calabria (southern Italy): new constraints from raised paleoshorelines. Geomorphology 395, 107978. https://doi.org/10.1016/j.geomorph.2021.107978.

Cerrone, C., Vacchi, M., Fontana, A., Rovere, A., 2021b. Last Interglacial Sea-level proxies in the western Mediterranean. Earth Syst. Sci. Data 13, 4485–4527. https://doi.org/10.5194/essd-13-4485-2021.

Chiarella, D., Capella, W., Longhitano, S.G., Muto, F., 2021. Fault-controlled base-of-scarp deposits. Basin Res. 33, 1056–1075. https://doi.org/10.1111/bre.12505.

Contreras, J., Anders, M.H., Scholz, C.H., 2000. Growth of a normal fault system : observations from the Lake Malawi basin of the east african rift. J. Struct. Geol. 22, 159–168. https://doi.org/10.1016/S0191-8141(99)00071-1.

Cowie, P.A., 1998. A healing–reloading feedback control on the growth rate of seismogenic faults. J. Struct. Geol. 20 https://doi.org/10.1016/S0191-8141(98)00034-0.

Cowie, P.A., Phillips, R.J., Roberts, G.P., McCaffrey, K.J.W., Zijerveld, L.J.J., Gregory, L. C., Faure Walker, J.P., Wedmore, L.N.J., Dunai, T.J., Binnie, S.A., Freeman, S.P.H.T., Wilcken, K., Shanks, R.P., Huismans, R.S., Papanikolaou, I., Michetti, A.M., Wilkinson, M., 2017. Orogen-scale uplift in the central Italian Apennines drives episodic behaviour of earthquake faults. Sci. Rep. 7, 44858. https://doi.org/ 10.1038/srep44858.

Cowie, P.A., Roberts, G.P., 2001. Constraining slip rates and spacings for active normal faults. J. Struct. Geol. 23, 1901–1915. https://doi.org/10.1016/S0191-8141(01) 00036-0.

Cowie, P.A., Roberts, G.P., Bull, J.M., Visini, F., 2012. Relationships between fault geometry, slip rate variability and earthquake recurrence in extensional settings. Geophys. J. Int. 189, 143–160. https://doi.org/10.1111/j.1365-246X.2012.05378.x.

Cowie, P.A., Shipton, Z.K., 1998. Fault tip displacement gradients and process zone dimensions. J. Struct. Geol. 20, 983–997. https://doi.org/10.1016/S0191-8141(98) 00029-7.

Cowie, P.A., Underhill, J., Behn, M., Lin, J., Gill, C., 2005. Spatio-temporal evolution of strain accumulation derived from multi-scale observations of late Jurassic rifting in the northern North Sea: a critical test of models for lithospheric extension. Earth Planet. Sci. Lett. 234, 401–419. https://doi.org/10.1016/j.epsl.2005.01.039.

Crémière, A., Lepland, A., Chand, S., Sahy, D., Condon, D.J., Noble, S.R., Martma, T., Thorsnes, T., Sauer, S., Brunstad, H., 2016. Timescales of methane seepage on the norwegian margin following collapse of the Scandinavian Ice Sheet. Nat. Commun. 7, 11509. https://doi.org/10.1038/ncomms11509.

De Guidi, G., Catalano, S., Monaco, C., Tortorici, L., 2003. Morphological evidence of Holocene coseismic deformation in the Taormina region (NE Sicily). J. Geodyn. 36, 193–211. https://doi.org/10.1016/S0264-3707(03)00047-4.

De Guidi, G., Catalano, S., Monaco, C., Tortorici, L., Di Stefano, A., 2002. Long-term effects of late Quaternary normal faulting in southern Calabria and eastern Sicily. Studi Geol. Camerti 1, 79–93.

De Santis, V., Scardino, G., Meschis, M., Ortiz, J.E., Sánchez-Palencia, Y., Caldara, M., 2021. Refining the middle-late Pleistocene chronology of marine terraces and uplift history in a sector of the Apulian foreland (southern Italy) by applying a synchronous correlation technique and amino acid racemization to Patella spp. and Thetystrombus latus. Ital. J. Geosci. 140. https://doi.org/10.3301/IJG.2021.05.

Doglioni, C., Ligi, M., Scrocca, D., Bigi, S., Bortoluzzi, G., Carminati, E., Cuffaro, M., D'Oriano, F., Forleo, V., Muccini, F., Riguzzi, F., 2012. The tectonic puzzle of the Messina area (Southern Italy): insights from new seismic reflection data. Sci. Rep. 2, 970. https://doi.org/10.1038/srep00970.

Dumas, B., Guérémy, P., Raffy, J., 2005. Evidence for sea-level oscillations by the "characteristic thickness" of marine deposits from raised terraces of Southern Calabria (Italy). Quat. Sci. Rev. 24, 2120–2136. https://doi.org/10.1016/j. quascirev.2004.12.011.

Dumas, B., Raffy, J., 2004. Late Pleistocene tectonic activity deduced from uplifted marine terraces in Calabria, facing the Strait of Messina. Quaternaria Nova 8, 79–99.

Ferranti, L., Antonioli, F., Mauz, B., Amorosi, A., Dai Pra, G., Mastronuzzi, G., Monaco, C., Orrù, P., Pappalardo, M., Radtke, U., Renda, P., Romano, P., Sansò, P., Verrubbi, V., 2006. Markers of the last interglacial sea-level high stand along the coast of Italy: tectonic implications. Quat. Int. 145–146, 30–54. https://doi.org/ 10.1016/j.quaint.2005.07.009.

Ferranti, L., Monaco, C., Antonioli, F., Maschio, L., Kershaw, S., Verrubbi, V., 2007. The contribution of regional uplift and coseismic slip to the vertical crustal motion in the Messina Straits, southern Italy: evidence from raised late Holocene shorelines. J. Geophys. Res. 112, B06401 https://doi.org/10.1029/2006JB004473.

Ghisetti, F., 1984. In: Recent Deformations and the Seismogenic Source in the Messina Strait (Southern Italy), 109, pp. 191–208. https://doi.org/10.1016/0040-1951(84) 90140-9.

González-Alfaro, J., Vargas, G., Ortlieb, L., González, G., Ruiz, S., Báez, J.C., Mandeng-yogo, M., Caquineau, S., Álvarez, G., 2018. Abrupt increase in the coastal uplift and earthquake rate since ~40 ka at the northern Chile seismic gap in the Central Andes. Earth Planet. Sci. Lett. 502, 32–45. https://doi.org/10.1016/j.epsl.2018.08.043.

Gupta, S., Cowie, P.A., Dawers, N.H., Underhill, J.R., 1998. A mechanism to explain rift-basin subsidence and stratigraphic patterns through fault-array evolution. Geology 26, 595–598. https://doi.org/10.1130/0091-7613(1998)026<0595:AMTERB>2.3. CO;2.

Gvirtzman, Z., Nur, A., 1999a. Plate detachment, asthenosphere upwelling, and topography across subduction zones. Geology 27, 563. https://doi.org/10.1130/ 0091-7613(1999)027<0563:PDAUAT>2.3.CO;2.

Gvirtzman, Z., Nur, A., 1999b. The formation of Mount Etna as the consequence of slab rollback. Nature 401, 782–785. https://doi.org/10.1038/44555.

Houghton, S.L., Roberts, G.P., Papanikolaou, I.D., McArthur, J.M., 2003. New 234 U- 230 Th coral dates from the western Gulf of Corinth: Implications for extensional tectonics. Geophys. Res. Lett. 30, 2013. https://doi.org/10.1029/2003GL018112.

INGV - DISS Working Group, 2018. Database of Individual Seismogenic Sources (DISS), Version 3.2.1: A Compilation of Potential Sources for Earthquakes Larger Than M 5.5 in Italy and Surrounding Areas. https://doi.org/10.6092/INGV.IT-DISS3.2.1.

Lajoie, K.R., 1986. Coastal tectonics. In: Active Tectonics: Impact on Society, pp. 95–124.

Maesano, F.E., Tiberti, M.M., Basili, R., 2017. The Calabrian Arc: three-dimensional modelling of the subduction interface. Sci. Rep. 7, 1–15. https://doi.org/10.1038/ s41598-017-09074-8.

Malinverno, A., Ryan, W.B.F., 1986. Extension in the Tyrrhenian Sea and shortening in the Apennines as result of arc migration driven by sinking of the lithosphere. Tectonics 5, 227–245. https://doi.org/10.1029/TC005i002p00227.

Martín-Banda, R., Insua-Arévalo, J.M., García-Mayordomo, J., 2021. Slip rate variation during the last ~210 ka on a slow fault in a transpressive regime: the Carrascoy Fault (Eastern Betic Shear Zone, SE Spain). Front. Earth Sci. 8, 1–21. https://doi.org/ 10.3389/feart.2020.599608.

Mcleod, A.E., Dawers, N.H., Underhill, J.R., 2000. The propagation and linkage of normal faults : insights from the Strathspey – Brent – Statfjord fault array, northern North Sea. Basin Res. 12, 263–284.

Meschis, M., Roberts, G.P., Mildon, Z.K., Robertson, J., Michetti, A.M., Faure Walker, J. P., 2019. Slip on a mapped normal fault for the 28th December 1908 Messina earthquake (Mw 7.1) in Italy. Sci. Rep. 1–8. https://doi.org/10.1038/s41598-019-42915-2.

Meschis, M., Roberts, G.P., Robertson, J., Briant, R.M., 2018. The relationships between regional quaternary uplift, deformation across active Normal Faults, and Historical Seismicity in the Upper Plate of Subduction zones: the Capo D'Orlando Fault, NE Sicily. Tectonics 37, 1231–1255. https://doi.org/10.1029/2017TC004705.

Meschis, M., Scicchitano, G., Roberts, G.P., Robertson, J., Barreca, G., Monaco, C., Spampinato, C., Sahy, D., Antonioli, F., Mildon, Z.K., Scardino, G., 2020. Regional deformation and offshore crustal local faulting as combined processes to explain uplift through time constrained by investigating differentially-uplifted Late Quaternary palaeoshorelines: the foreland Hyblean Plateau, SE Sicily. Tectonics. https://doi.org/10.1029/2020TC006187.

Mildon, Z.K., Roberts, G.P., Faure Walker, J.P., Beck, J.W., Papanikolaou, I.D., Michetti, A.M., Toda, S., Campbell, L., McCaffrey, K.J.W., 2019. Earthquake Clustering Controlled by Shear Zone Interaction. https://doi.org/10.31223/osf.io/ qkx2v.

Miller, W.R., Mason, T.R., 1994. Erosional features of coastal beachrock and aeolianite outcrops in Natal and Zululand, South Africa. J. Coast. Res. 10, 374–394. https:// doi.org/10.2307/4298223.

Miyauchi, T., Dai Pra, G., Sylos Labini, S., 1994. Geochronology of Pleistocene marine terraces and regional tectonics in the Tyrrhenian coast of South Calabria, Italy. Il Quaternario 7, 17–34.

Monaco, C., Tortorici, L., 2000. Active faulting in the Calabrian arc and eastern Sicily. J. Geodyn. 29, 407–424. https://doi.org/10.1016/S0264-3707(99)00052-6.

Nicol, A., Walsh, J.J., Berryman, K., Villamor, P., 2006. Interdependence of fault displacement rates and paleoearthquakes in an active rift. Geology 34, 865–868. https://doi.org/10.1130/G22335.1.

Ott, R.F., Gallen, S.F., Wegmann, K.W., Biswas, R.H., Herman, F., Willett, S.D., 2019. Pleistocene terrace formation, Quaternary rock uplift rates and geodynamics of the Hellenic Subduction Zone revealed from dating of paleoshorelines on Crete, Greece. Earth Planet. Sci. Lett. 525, 115757 https://doi.org/10.1016/j.epsl.2019.115757.

Pavano, F., Pazzaglia, F.J., Catalano, S., 2016. Knickpoints as geomorphic markers of active tectonics: a case study from northeastern Sicily (southern Italy). Lithosphere 8, 633–648. https://doi.org/10.1130/L577.1.

Pedoja, K., Jara-Muñoz, J., De Gelder, G., Robertson, J., Meschis, M., Fernandez-Blanco, D., Nexer, M., Poprawski, Y., Dugué, O., Delcaillau, B., Bessin, P., Benabdelouahed, M., Authemayou, C., Husson, L., Regard, V., Menier, D., Pinel, B., 2018. Neogene-Quaternary slow coastal uplift of Western Europe through the perspective of sequences of strandlines from the Cotentin Peninsula (Normandy, France). Geomorphology 303, 338–356. https://doi.org/10.1016/j. geomorph.2017.11.021.

Quye-sawyer, J., Whittaker, A.C., Roberts, G., Rood, D., 2021. Fault throw and regional uplift histories from drainage analysis : evolution of Southern Italy. Tectonics 40. https://doi.org/10.1029/2020TC006076.

Roberts, G.P., Houghton, S.L., Underwood, C., Papanikolaou, I., Cowie, P.A., Van Calsteren, P., Wigley, T., Cooper, F.J., McArthur, J.M., 2009. Localization of quaternary slip rates in an active rift in 105 years: an example from Central Greece constrained by 234U–230Th coral dates from uplifted paleoshorelines. J. Geophys. Res. Solid Earth 114, 1–26. https://doi.org/10.1029/2008JB005818.

Roberts, G.P., Meschis, M., Houghton, S., Underwood, C., Briant, R.M., 2013. The implications of revised Quaternary palaeoshoreline chronologies for the rates of active extension and uplift in the upper plate of subduction zones. Quat. Sci. Rev. 78, 169–187. https://doi.org/10.1016/j.quascirev.2013.08.006.

Roberts, G.P., Michetti, A.M., 2004. Spatial and temporal variations in growth rates along active normal fault systems: an example from the Lazio-Abruzzo Apennines, Central Italy. J. Struct. Geol. 26, 339–376. https://doi.org/10.1016/S0191-8141(03) 00103-2.

Roberts, G.P., Michetti, A.M., Cowie, P., Morewood, N.C., Papanikolaou, I., 2002. Fault slip-rate variations during crustal-scale strain localisation, Central Italy. Geophys. Res. Lett. 29 https://doi.org/10.1029/2001GL013529, 9-1-9-4.

Robertson, J., Meschis, M., Roberts, G.P., Ganas, A., Gheorghiu, D.M., 2019. Temporally constant Quaternary Uplift rates and their relationship with Extensional Upper-Plate Faults in south Crete (Greece), constrained with 36Cl cosmogenic exposure dating. Tectonics 38. https://doi.org/10.1029/2018TC005410.

Robertson, J., Roberts, G.P., Iezzi, F., Meschis, M., Gheorghiu, D.M., Sahy, D., Bristow, C., Sgambato, C., 2020. Distributed normal faulting in the tip zone of the South Alkyonides Fault System, Gulf of Corinth, constrained using 36Cl exposure dating of late-Quaternary wave-cut platforms. J. Struct. Geol. 136, 104063 https:// doi.org/10.1016/j.jsg.2020.104063.

Roda-Boluda, D.C., Whittaker, A.C., 2017. Structural and geomorphological constraints on active normal faulting and landscape evolution in Calabria, Italy. J. Geol. Soc. https://doi.org/10.1144/jgs2016-097 jgs2016-097.

Rohling, E.J., Foster, G.L., Grant, K.M., Marino, G., Roberts, A.P., Tamisiea, M.E., Williams, F., 2014. Sea-level and deep-sea-temperature variability over the past 5.3 million years. Nature 508, 477–482. https://doi.org/10.1038/nature13230.

Saillard, M., Hall, S.R., Audin, L., Farber, D.L., Hérail, G., Martinod, J., Regard, V., Finkel, R., Bondoux, F., 2009. Non-steady long-term uplift rates and Pleistocene marine terrace development along the andean margin of Chile (31° S) inferred from 10 be dating. Earth Planet. Sci. Lett. 277, 50–63. https://doi.org/10.1016/j. epsl.2008.09.039.

Schiano, P., Clocchiatti, R., Ottolini, L., Busà, T., 2001. Transition of Mount Etna lavas from a mantle-plume to an island-arc magmatic source. Nature 412, 900–904. https://doi.org/10.1038/35091056.

Serpelloni, E., Bürgmann, R., Anzidei, M., Baldi, P., Mastrolembo Ventura, B., Boschi, E., 2010. Strain accumulation across the Messina Straits and kinematics of Sicily and Calabria from GPS data and dislocation modeling. Earth Planet. Sci. Lett. 298, 347–360. https://doi.org/10.1016/j.epsl.2010.08.005.

Sgambato, C., Faure Walker, J.P., Mildon, Z.K., Roberts, G.P., 2020. Stress loading history of earthquake faults influenced by fault/shear zone geometry and Coulomb pre-stress. Sci. Rep. 10, 12724. https://doi.org/10.1038/s41598-020-69681-w.

Sgroi, T., Polonia, A., Barberi, G., Billi, A., Gasperini, L., 2021. New seismological data from the Calabrian arc reveal arc-orthogonal extension across the subduction zone. Sci. Rep. 11, 473. https://doi.org/10.1038/s41598-020-79719-8.

Shikakura, Y., 2014. Marine terraces caused by fast steady uplift and small coseismic uplift and the time-predictable model: case of Kikai Island, Ryukyu Islands, Japan. Earth Planet. Sci. Lett. 404, 232–237. https://doi.org/10.1016/j.epsl.2014.08.003.

Shyu, J.B.H., Wang, C., Wang, Y., Shen, C., Chiang, H., Liu, S., Min, S., Thu, L., Than, O., Thura, S., 2018. Upper-plate splay fault earthquakes along the Arakan subduction belt recorded by uplifted coral microatolls on northern Ramree Island, western Myanmar (Burma). Earth Planet. Sci. Lett. 484, 241–252. https://doi.org/10.1016/j.epsl.2017.12.033.

Siddall, M., Rohling, E.J., Almogi-Labin, A., Hemleben, C., Meischner, D., Schmelzer, I., Smeed, D.A., 2003. Sea-level fluctuations during the last glacial cycle. Nature 423, 853–858. https://doi.org/10.1038/nature01690.

Spampinato, C.R., Ferranti, L., Monaco, C., Scicchitano, G., Antonioli, F., 2014. Raised Holocene paleo-shorelines along the Capo Vaticano coast (western Calabria, Italy): evidence of co-seismic and steady-state deformation. J. Geodyn. 82, 178–193. https://doi.org/10.1016/j.jog.2014.03.003.

Spampinato, C.R., Scicchitano, G., Ferranti, L., Monaco, C., 2012. Raised Holocene paleo-shorelines along the Capo Schisò coast, Taormina: new evidence of recent co-seismic deformation in northeastern Sicily (Italy). J. Geodyn. 55, 18–31. https://doi.org/10.1016/j.jog.2011.11.007.

Stewart, I.S., Cundy, A., Kershaw, S., Firth, C., 1997. Holocene coastal uplift in the taormina area, northeastern sicily: implications for the southern prolongation of the calabrian seismogenic belt. J. Geodyn. 24, 37–50. https://doi.org/10.1016/S0264-3707(97)00012-4.

Tarquini, S., Vinci, S., Favalli, M., Doumaz, F., Fornaciai, A., Nannipieri, L., 2012. Release of a 10-m-resolution DEM for the italian territory: comparison with global-coverage DEMs and anaglyph-mode exploration via the web. Comput. Geosci. 38, 168–170. https://doi.org/10.1016/j.cageo.2011.04.018.

Valensise, G., Pantosti, D., 1992. A 125 Kyr-long geological record of seismic source repeatability: the Messina Straits (southern Italy) and the 1908 earthquake (M s 7/2). Terra Nova 4, 472–483. https://doi.org/10.1111/j.1365-3121.1992.tb00583.x.

Waelbroeck, C., Labeyrie, L., Michel, E., Duplessy, J.C., McManus, J.F., Lambeck, K., Balbon, E., Labracherie, M., 2002. Sea-level and deep water temperature changes derived from benthic foraminifera isotopic records. Quat. Sci. Rev. 21, 295–305. https://doi.org/10.1016/S0277-3791(01)00101-9.

Westaway, R., 1993. Quaternary uplift of southern Italy. J. Geophys. Res. 98, 741–772. https://doi.org/10.1029/93JB01566.